View metadata, citation and similar papers at core.ac.uk
brought to you by CORE
provided by Scholarship@Claremont

Claremont Colleges
Scholarship @ Claremont

HMC Senior Theses

HMC Student Scholarship

2013

Simulations of Surfactant Driven Thin Film Flow

Shreyas Kumar
Harvey Mudd College

Recommended Citation

Kumar, Shreyas, "Simulations of Surfactant Driven Thin Film Flow" (2013). *HMC Senior Theses*. 63.
https://scholarship.claremont.edu/hmc_theses/63

This Open Access Senior Thesis is brought to you for free and open access by the HMC Student Scholarship at Scholarship @ Claremont. It has been accepted for inclusion in HMC Senior Theses by an authorized administrator of Scholarship @ Claremont. For more information, please contact scholarship@cuc.claremont.edu.

Simulations of Surfactant Driven Thin Film Flow

Shreyas Kumar

Rachel Levy, Advisor

Darryl Yong, Reader

HARVEY
MUDD
COLLEGE

Department of Mathematics

May, 2014

Copyright © 2014 Shreyas Kumar.

The author grants Harvey Mudd College and the Claremont Colleges Library the nonexclusive right to make this work available for noncommercial, educational purposes, provided that this copyright statement appears on the reproduced materials and notice is given that the copying is by permission of the author. To disseminate otherwise or to republish requires written permission from the author.

Abstract

This thesis is intended to fulfill the requirements of the Math and Physics departments at Harvey Mudd College. We begin with a brief introduction to the study of surfactant dynamics followed by some background on the experimental framework our work is related to. We then go through a derivation of the model we use, and explore in depth the nature of the Equation of State (EoS), the relationship between the surface tension on a fluid and the surfactant concentration. We consider the effect of using an empirical equation of state on the results of the simulations and compare the new results against the results produced using a multilayer (EoS) as well as experimental observations. We find that the empirical EoS leads to two new behaviors - preserving of large gradients of surfactant concentration and the occurrence of dynamics in distinct regimes. These behaviors suggest that the empirical EoS improves the agreement of the model's prediction with experiment.

Contents

Abstract **iii**

Acknowledgments **ix**

1 Introduction **1**

2 The Experiment **3**
2.1 Some Physical Intuition 3
2.2 Key Components of the Experiment 5

3 The Model **9**
3.1 The Model for a Viscous Fluid 9

4 Numerics **21**
4.1 Implicit Solvers by Claridge, Levy and Wong 21

5 Experimental Factors that Inform the Model **25**
5.1 The Equation of State 25
5.2 Nondimensionalizing the Equations 29

6 Simulation Results **33**
6.1 Investigating the Impact of the EoS 33

7 Conclusion **53**
7.1 Summary of Results 53
7.2 Future Work 54

A Defining the Problem for the Implicit Solver **57**

Bibliography **59**

List of Figures

2.1 Initial conditions used in the lab. 4
2.2 The alveolus of the human lung with the three components pertinent to our model 5
2.3 A diagram of a monolayer of surfactant on the surface of the liquid with micelles present in the bulk. In our experiments we avoid the formations of micelles by ensuring the initial surfactant concentration is below the critical micelle concentration. 7

3.1 Initial conditions used in inward simulations. 18
3.2 Initial conditions used in outward simulations. 18

5.1 The linear equation of state 26
5.2 Different Equations of State with Stephen Strickland's data in red. 27
5.3 The multilayer and empirical EoS with their derivatives. Note that the exact values are not the same as those used in the simulations, though the general shape is the same. 28
5.4 The empirical EoS can be divided into three regions based on the value of its derivative (whether the derivative is nonzero or not). This division will be referred to in Section 6 to interpret the simulated profiles. 29
5.5 Fitting a functional form to experimental data collected at NCSU. Note the similarity in the fits and residuals. 32

6.1 A slice at $\theta = 0$ of the height profile in blue with the azimuthally averaged profile in black. We see perfect agreement. 34
6.2 Verifying conservation of mass and surfactant 35
6.3 Surfactant profiles for the multilayer and empirical EoS at $0.6\,\Gamma_c$. 37

6.4 Surfactant profiles from experimental runs carried out at the Daniels Non-Linear Lab at NCSU. We see steep surfactant gradients similar to those produced by the empirical EoS. Strickland et al. (2014) 38
6.5 Height profiles for the multilayer and empirical EoS at 0.6 Γ_c. 39
6.6 Surfactant profiles for the multilayer and empirical EoS with $\Gamma_0 = 0.8\Gamma_c$. 40
6.7 Height profiles for the multilayer and empirical EoS with $\Gamma_0 = 0.8\Gamma_c$. 41
6.8 The surfactant profiles at different Γ_0 for empirical EoS. . . . 42
6.9 The surfactant profiles at different Γ_0 for multilayer EoS. The dynamics hasten as Γ_0 increases but in a uniform way. There is no transition to a different regime. 43
6.10 Analyzing the leading edge of the surfactant in inward spreading runs using the empirical EoS. 44
6.11 Analyzing the height of the central distension in inward spreading runs using the empirical EoS. 45
6.12 Surfactant profiles for the multilayer and empirical EoS. . . . 47
6.13 Height profiles for the multilayer and empirical EoS. 48
6.14 Analyzing the leading edge of surfactant for the empirical EoS in outward spreading runs. 49
6.15 Outward spreading runs for $\Gamma_0 = \Gamma_c$ and $\Gamma_0 = 3\Gamma_c$ 50

Acknowledgments

I would like to thank my advisor Professor Rachel Levy, second reader Professor Darryl Yong, fellow thesis student Peter Megson and all the other members of the Levylab group. I would also like to thank Jonathan Claridge and Jeffrey Wong for the invaluable help with the numerics, Cameron Gaebler for help with running simulations and Stephen Strickland for all his data and help with the experiments.

Chapter 1

Introduction

Surfactant-driven dynamics on thin liquid films has been a rich area of study in applied mathematics since the 1990's. One reason to study surfactant-driven flow is that it plays an important part in the respiration process—the alveolar wall in the human lung is a surfactant-driven thin film system. The alveolar wall is covered by a layer of mucus (a thin film), which usually has DPPC [1], a surfactant, on its surface. When babies are born prematurely, the DPPC-producing cells in the lungs are often underdeveloped. Present treatment involves intubating the babies and forcing a bolus of surfactant down their lungs. This method does not always work, and when it fails it can prove fatal to the infant. A hypothesis for why the surfactant delivery mechanism fails is that the surfactant does not pass through all the airways down to the alveoli. This research aims to better understand surfactant spreading in the hope that we can eventually improve the surfactant delivery mechanism.

In addition to the long term goal of aiding delivery mechanisms for pulmonary surfactant, surfactant-driven flow on thin films is a physical phenomenon that exhibits very interesting behavior and has numerous industrial applications. By performing experiments and developing a model to describe surfactant-driven flow, we hope to gain some amount of predictive ability. An important step in posing the surfactant-driven thin film flow as a mathematical problem is to relate the surface tension of a fluid to the surfactant concentration. This relation is exceedingly important as it describes how the surfactant 'drives' the fluid. In this thesis, we consider the effect of an empirically determined relation on the results of the simulations of the model. We compare the results to a previously used (non-empiric) relation, and interpret the results in the context of experimental observations. We find that the empiric relation improves our model's agreement with experiments in certain important respects, though further work is necessary to fully understand the impact of this relation.

---

[1] DPPC stands for dipalmitoylphosphatidylcholin and is a phospholipid that is the major constituent of pulmonary surfactant.

Chapter 2

The Experiment

2.1 Some Physical Intuition

In the Summer and Fall of 2013, our group spent a considerable amount of time setting up the surfactant spreading experiments at Harvey Mudd College and learning how to operate it. With the help of Stephen Strickland, a PhD student at NC State University, we ported over an experimental setup conceptualized at the Daniels Non-Linear Lab at NC State University while automating several aspects of the experimental setup. Working on the experiments provided me with some physical intuition that was invaluable while working with the simulations. So, before we extensively explore the surfactant thin-film model, I believe it would be useful to go through the experimental setup to better understand the system. This should also prove useful when comparing some of the simulation results to experimental observations in Chapter 6.

2.1.1 The Setup

This section will provide a general overview of the experiment and data collection. Further details of the experimental procedures and data analysis can be found in Peter Megson's thesis (Megson, 2014). The experiment was designed to create a reproducible initial condition, and record the dynamics as the system evolves in time. Two initial conditions are chosen: inward spreading and outward spreading. In both cases a ring of radius 3 cm is used to separate the spatial domain into two distinct regions, the inside and the outside. Depending on whether the run is inward or outward spreading, one of the two regions is filled with surfactant (this will be dis-

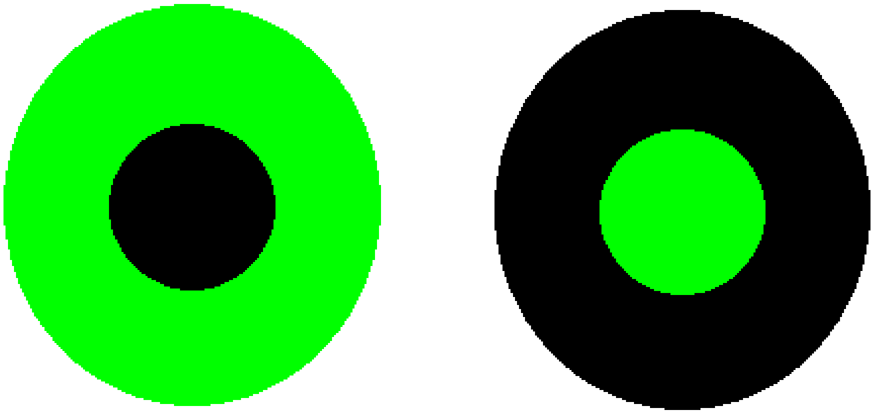

a. The initial condition for inward spreading runs: high surfactant concentration in an annular region with no surfactant in a central disk.

b. The initial condition for outward spreading runs: high surfactant concentration in a central disk with no surfactant in the surrounding annular region.

Figure 2.1 Initial conditions used in the lab.

cussed in greater detail in Chapter 6). A top-down view of these two initial conditions is presented in Figure 2.1 where the green represents a region of high surfactant concentration while the black represents a region of low surfactant concentration. The surfactant is deposited on a thin film ($\tilde{1}$mm) of glycerol. Once the surfactant and glycerol are deemed to have reached equilibrium (i.e. uniformly spread out), the ring is lifted and the system is allowed to evolve. The glycerol takes about an hour and a half to reach equilibrium, while the surfactant takes about a half hour to do the same. In the inward spreading case, we see the fluid and surfactant moving inward, while in the outward spreading case we see the fluid and surfactant moving outward.

2.1.2 Limitations of Data Collection

The data collection in the experiments extracts two pieces of information from images of the system evolving—the height of the film and the surfactant concentration profile. This information is important since the predominant model that describes surfactant-driven flow can be described in terms of two equations, one each for the height and surfactant concentration (the details of the model can be found in Chapter 3). While the details of the data collection are beyond the scope of this thesis, it is important to note that the data collection techniques used require the height and surfactant profiles to be azimuthally symmetric. Furthermore, experimentally, we have observed that our profiles are azimuthally symmetric when we start with a symmetric initial condition. This motivates our choice of azimuthally symmetric initial conditions in the simulations.

2.2 Key Components of the Experiment

The goal of modeling any physical phenomenon is to pose the problem in a mathematical framework. To pose our experiment as a mathematical problem, we need to identify the key components of the experiment so we can explicitly account for them in the model. In this experiment, we identify three important components: the substrate, the fluid and the surfactant. Each of these components bear closer scrutiny.

As stated in Chapter 1, the long-term motivation of the project is to study the surfactant dynamics in the context of their role in the human respiration process. So, we need to understand the simplifications our model makes with respect to the alveolar wall of the lungs; this would help us eventually move toward a model that is more directly applicable to surfactant-replacement therapy.

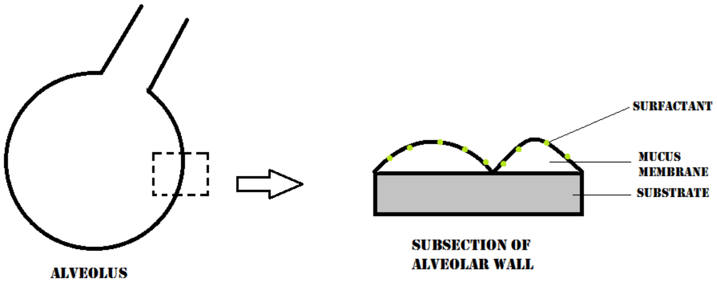

Figure 2.2 The alveolus of the human lung with the three components pertinent to our model

2.2.1 The Substrate

In the lung, the substrate is the alveolar wall. This is a highly non-uniform, ciliated surface and proves to be very difficult to model or recreate in a lab setting. Mathematically, the substrate determines the geometry of the boundary at the lower surface of the fluid and the flux conditions there. Applying boundary conditions on complex geometries is difficult,and computationally expensive. Incorporating such a boundary into an experiment is even more difficult; instead, in the lab, we use a rigid aluminum well with a silicon wafer on top of it as the substrate. Consequently, we stick to a rigid, impermeable boundary on the lower surface in the model as well.

2.2.2 The Fluid

The ultimate goal of our research group is to understand surfactant-driven dynamics on mucus, which is a viscoelastic fluid. Modeling viscoelastic fluids has proven challenging, and hence many present models for surfactant-driven flow are developed over viscous fluids. Previous experimentation and modeling has used glycerine as the underlying film. This thesis investigates the agreement between experiment and simulations for the model developed for a viscous fluid. From a mathematical perspective, using a viscous fluid allows us to use Navier-Stokes' Equations as a starting point; this greatly aids the modeling process.

2.2.3 The Surfactant

A surfactant is a chemical that when present in or on a liquid, reduces the surface tension. Hence, the presence of a surfactant concentration gradient creates a surface tension gradient, which in turn causes a surface stress. The surfaces stress then causes motion in the underlying liquid, and the surfactant is transported along with the bulk. The surface stresses which arise in the presence of surface tension gradients are termed Marangoni forces and will be a central aspect of study.

Since surfactants are complex chemicals it is important to understand how they interact with the bulk and the substrate. A surfactant usually has a hydrophyllic head and a hydrophobic tail—in DPPC (the surfactant found in the human lung), the PC chain is the hydrophyllic head. When the surfactant concentration is below a critical concentration level, the surfactant molecules are present as a monolayer on the surface—individual molecules with the tail oriented away from the surface and the head present at the film-air interface. At large concentrations, the surfactant molecules can form complicated structures like micelles and bilayers. Micelles are spheres of surfactant where all the tails are bunched together on the inside while the heads are oriented radially outward; in a bilayer, the surfactants form a two molecule sheet of surfactant where the tails are grouped in the middle of the layer and the heads are on the outside. A diagram of a monolayer of surfactant and micelles is presented in Figure 2.3. In our investigation of surfactant-driven dynamics, we are mostly focused on the first case, the monolayer, though we do briefly consider the effect of starting with a large initial surfactant concentration in Chapter 6.

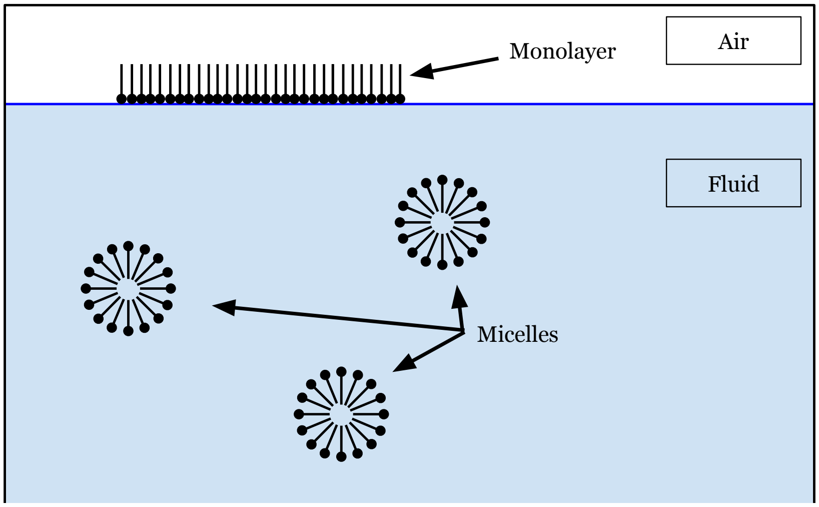

Figure 2.3 A diagram of a monolayer of surfactant on the surface of the liquid with micelles present in the bulk. In our experiments we avoid the formations of micelles by ensuring the initial surfactant concentration is below the critical micelle concentration.

It is also worthwhile to note that we restrict ourselves to insoluble surfactant. We further assume that all the chemical properties and variations between surfactants are captured by the relationship between the surfactant concentration and the surface tension (discussed in Chapter 5. The experimental data is collected using NBD-PC [1]. While this thesis is not concerned with the experiment per se, it is possible that replacing DPPC with

---

[1] NBD-PC stands for nitrobenzofuran-conjugated phosphatidylcholine. Here, a second fluorescent molecule is added to the PC tail of DPPC. This is fluorescent tail is central to extracting surfactant concentration data. Further details can be found in Peter Megson's senior thesis(Megson, 2014).

NBD-PC could have an effect on the dynamics, and hence comparisons. We try to make accurate comparisons between the experiment and the model by using a relation between surfactant concentration and surface tension that is specific to NBD-PC.

Chapter 3

The Model

3.1 The Model for a Viscous Fluid

Since this thesis aims to fulfill the requirements of both the Mathematics and Physics departments, I will go through the derivation of the model for surfactant-driven thin film flow on a viscous fluid in detail. This model was developed initially by Gaver and Grotberg (1990) though this particular derivation follows that presented by Ellen Swanson in her PhD thesis (Swanson, 2010). The general idea is to begin with the Navier-Stokes equations and apply some assumptions to reduce them to the Stokes equations. We then use the pressure and velocity fields with appropriate boundary conditions to extract a depth averaged velocity. Finally, we use conservation of mass and transport of surfactant to arrive at the governing equations in height and surfactant concentration.

3.1.1 Overarching Assumptions

By choosing a viscous fluid and and a uniform, rigid substrate, we have already made two important assumptions. There are three more assumptions that are central to this derivation. First, the Reynold's number (a dimensionless quantity that describes the level of turbulence the flow) is assumed to be very small, in other words, the flow is slow. Second, we assume that the flow is incompressible and third, we use the lubrication approximation. This approximation implies that the characteristic height of a fluid is much smaller than the characteristic length. These assumptions will be explained in greater detail at the points at which they are used in the derivation.

3.1.2 An Aside on Notation

We use Einstein tensor notation to facilitate deriving the governing equations. The Navier-Stokes equations are easier to manipulate using this tensor notation; once we obtain the necessary equations from Navier-Stokes, we revert to vector notation.

Let the basis set $\{x, y, z\}$ map to $\{x_1, x_2, x_3\}$. Next, any vector $\mathbf{v} = (v_1, v_2, v_3)$ will be denoted as just v_i. If there is a repeated index, this represents an implicit sum—so $v_i u_i = \sum_i v_i u_i = v_1 u_1 + v_2 u_2 + v_3 u_3$, the dot product of v and u. The final bit of notation pertains to the representation of derivatives—$\frac{\partial \mathbf{u}}{\partial x_1}$ is represented as $u_{i,1}$. If there is more than one derivative, they are applied in the order from left to right. So $\frac{\partial^2 \mathbf{u}}{\partial x_2 \partial x_1}$ would be $u_{i,12}$.

Here is a list of common operations listed in vector notation with its analog in Einstein tensor notation. $\mathbf{u}$ and $\mathbf{v}$ are vectors, ϵ_{ijk} is the Levi-Civita rank-3 tensor and δ_{ij} is the Kronecker delta. ϵ_{ijk} and δ_{ij} are defined below.

$$\delta_{ij} = \begin{cases} 1 & \text{if } i = j \\ 0 & \text{if } i \neq j \end{cases}$$

$$\epsilon_{ijk} = \begin{cases} 1 & \text{if } (i,j,k) = (1,2,3), (3,1,2), (2,3,1) \\ -1 & \text{if } (i,j,k) = (1,3,2), (3,2,1), (2,1,3) \\ 0 & \text{otherwise} \end{cases}$$

$$\mathbf{u} \cdot \mathbf{v} = u_i v_i \qquad \nabla \mathbf{u} = u_{i,j} \qquad \nabla \cdot \mathbf{u} = u_{i,i}$$
$$\nabla \times \mathbf{u} = \epsilon_{ijk} u_{j,k} \qquad \Delta \mathbf{u} = u_{i,jj}.$$

Also, if we have a scalar f, then $\nabla f = f_{,i}$. As an example, we show how we derive the tensor representation of the vector Laplacian.

$$\Delta u = \nabla \cdot (\nabla u) = \nabla \cdot (u_{i,j}) = (u_{i,j})_{,j} = u_{i,jj}$$

3.1.3 Simplifying Navier-Stokes

We consider a fluid which has an arbitrary velocity profile. Let u_i represent the velocity vector, where u_i can be dependent on x_i and t (where t is time) so $\mathbf{u} = \mathbf{u}(x_i, t)$. The dynamics of any Newtonian fluid are described by the Navier-Stokes equations. The Navier-Stokes equation are presented below (Lyzenga and Bernoff, 2013).

$$\rho F_i + \Pi_{im,m} = \rho \frac{du_i}{dt} \tag{3.1}$$

$$\dot{\rho} + (\rho u_m)_{,m} = 0 \tag{3.2}$$

$$\Pi_{ij} = (-p + \eta u_{n,n})\delta_{ij} + \mu(u_{i,j} + u_{j,i}). \tag{3.3}$$

In the equations above, ρ is the mass density, Π_{ij} is the stress tensor, u the velocity field, p is the pressure and F_i is any external force (per unit mass) on the system. η and μ are the two kinds of viscosities—with μ being the kinematic viscosity and η the bulk viscosity. Also, the over-dot in $\dot{p}$ represents a derivative with respect to time. Usually, these equations are complete on their own. In our case we have an additional relation that accounts for the effect of the surfactant—this will be explored later.

We begin by applying the incompressibility condition—this tells us that the density is contant with time. Consequently Equation 3.2 becomes

$$\rho u_{n,n} = 0 \implies u_{n,n} = 0. \tag{3.4}$$

In other words, the velocity field is divergence free. In the two-dimensional case, this translates to

$$u_{1,1} + u_{2,2} + u_{3,3} = 0. \tag{3.5}$$

We now notice that the divergence of u is present in the stress strain relation in Equation 3.3. We can now simplify the stress strain relation by using Equation 3.4

$$\Pi_{ij} = -p\delta_{ij} + \mu(u_{i,j} + uj, i). \tag{3.6}$$

Next, we substitute Π_{ij} from Equation 3.6 into Equation 3.1. This gives us,

$$\rho F_i + ((-p\delta_{ij} + \mu(u_{i,j} + u_{j,i}))_{,j} = \rho \dot{u}_i + \rho u_{i,n} u_n. \tag{3.7}$$

Note that we have expanded out the full derivative of u with respect to time using the chain rule. Simplifying this further,

$$\rho F_i - p_{,j} + u_{i,jj} + u_{j,ij} = \rho \dot{u}_i + \rho u_{i,n} u_n. \tag{3.8}$$

Since we can reorder the partial derivatives on the velocity, the term $u_{j,ij} = u_{j,ji}$ is the gradient of the divergence and that, again, is zero. Dropping that term,

$$\rho F_i - p_{,j} + u_{i,jj} = \rho \dot{u}_i + \rho u_{i,n} u_n. \tag{3.9}$$

Next, we consider the external forcing term F_i; in this system the only external force present is gravity. For generality, we introduce a parameter α

which is defined to be the angle of incline of the substrate. The force due to gravity is then (confining ourselves to the $x - z$ plane)

$$\mathbf{F} = (g \sin \alpha, 0, -g \cos \alpha)$$

with g being the regular acceleration due to gravity. Since we are confining ourselves to two-dimensions, Equation 3.7 should result in three equations—one for each component of the velocity profile. Switching to regular vector notation Equation 3.8 becomes

$$\rho F_i - p_{,i} + u_{i,jj} = \rho_i \dot{u}_i + \rho u_n u_{i,n}. \tag{3.10}$$

It is now appropriate to apply our first assumptions—that is the flow is slow. In other words the Reynolds number $Re = \frac{\rho L U}{\mu} \ll 1$ (where L and U are characteristic length and velocity scales which will be defined soon). In this regime it is fair to assume that the convective acceleration term is negligible compared to the $\dot{\mathbf{u}}$ term. An in depth discussion of the relative magnitude of this term in a low Reynolds number regime can be found in *Fields and Waves* by Lyzenga and Bernoff (2013). We now arrive at the Stokes' equations; they are the linearized version of the Navier-Stokes equations as the non-linear convective term is absent.

$$\rho F_i - p_{,i} + u_{i,jj} = \rho \dot{u}_i. \tag{3.11}$$

Before we move on to non-dimensionalizing the above system, it is worth considering the external forcing vector F_i in greater detail. If we were to be completely general, we would assume an arbitrary angle of inclination α. Since all the experimental data we will compare this against is going to be in the $x - y$ plane or $\alpha = 0$, we assume that the forcing vector $\mathbf{F} = (0, -g, 0)$. It is not difficult to generalize this derivation to incorporate arbitrary α.

3.1.4 Non-Dimensionalizing this System

Non-dimensionalizing a system is extremely useful and important when one intends to numerically solve a system. This has two advantages—the quantities are now measured with respect to a scale that is intrinsic to the system as opposed to some arbitrary scale (such as the SI units). The second advantage is that code written for non-dimensionalized systems is usually more flexible and versatile'. In order to non-dimensionalize this equation, we need to define a some characteristic quantities. Below L, W and H represent the characteristic length scales in the x, y and z directions. Note that v is the projection of the velocity, $\mathbf{u}$ on to the $x - y$ plane.

$$x = L\hat{x} \qquad y = W\hat{y} \qquad z = H\hat{z} \qquad v = U\hat{v}.$$

An implicit assumption in the above definitions is that the velocity in both the x and y directions have the same characteristic length scales. We now apply the thin film approximation. The thin film approximation assumes that the parameter $H/L \equiv \epsilon \ll 1$. In other words the characteristic length scale of the fluid is much larger than the characteristic height scale. In our specific case, the film is usually about a few millimeters tall while it is tens of centimeters across, making this assumption valid. Furthermore, for simplicity we restrict the velocity field to be in just two dimensions, x and z. This derivation is, again, easily generalized to all three dimensions and it is carried out in an analogous manner. Setting $u_2 = 0$, the Stokes equations become

$$\rho F_i - p_{,i} + v_{i,jj} = \rho \dot{v}_i \tag{3.12}$$

$$v_{i,i} = 0. \tag{3.13}$$

Implementing the scalings described in Equation 3.5,

$$\frac{U}{L}\hat{u}_{\hat{1}} + \frac{1}{H}\hat{u}_{\hat{3}} = 0. \tag{3.14}$$

We now balance the terms on u_3 to get

$$u_3 = \frac{UH}{L}\hat{u}_{\hat{3}} = \epsilon U \hat{u}_{\hat{3}}. \tag{3.15}$$

With this scaling for u_3, we substitute the dimensionless quantities into the Stokes equations.

$$-\frac{1}{L}p_{\hat{1}} + U(\frac{1}{L^2}\hat{u}_{1,\hat{1}\hat{1}} + \frac{1}{H^2}\hat{u}_{3,\hat{3}\hat{3}}) = \rho U \dot{u}_1 \tag{3.16}$$

$$\rho g - \frac{1}{H}p_{\hat{1}} + U(\frac{1}{L^2}\hat{u}_{1,\hat{1}\hat{1}} + \frac{1}{H^2}\hat{u}_{3,\hat{3}\hat{3}}) = \rho U \dot{u}_3. \tag{3.17}$$

Rewriting these in terms of ϵ,

$$-\epsilon H p_{\hat{1}} + U(\epsilon^2 \hat{u}_{1,\hat{1}\hat{1}} + \hat{u}_{3,\hat{3}\hat{3}}) = 0 \tag{3.18}$$

$$H^2 \rho g - \epsilon H p_{\hat{1}} + U(\epsilon^2 \hat{u}_{1,\hat{1}\hat{1}} + \hat{u}_{3,\hat{3}\hat{3}}) = 0. \tag{3.19}$$

This yields the following pressure scaling,

$$p = P_0 \hat{p}, \qquad P_0 = \frac{\mu U}{\epsilon H}$$

Implementing this scaling, and keeping terms to first order, we arrive at the following set of equations (in dimensional coordinates),

$$p_1 = \mu u_{33} \tag{3.20}$$

$$p_3 = -\rho g. \tag{3.21}$$

3.1.5 Applying Boundary Conditions

We introduce the first unknown that we are interested in, the height of the fluid. This takes the form of a boundary condition at the surface, $h(x,t) = z$. Next, we apply the normal stress boundary condition, i.e. the normal stress on the surface balances the atmospheric pressure. So, at the surface,

$$p - p_{atm} = -\gamma\kappa. \tag{3.22}$$

Here κ is the curvature of the surface, p_{atm} is the atmospheric pressure and γ is the intrinsic surface tension of the fluid. To first order, we can approximate the curvature as $\kappa \approx h_{xx}$. This boundary condition becomes

$$p - p_{atm} = -\gamma h_{11}. \tag{3.23}$$

Next, we consider the tangential surface stress. The tangential surface stress is influenced by the surfactant concentration at the surface. We introduce the equation of state, $\sigma(\Gamma)$, to describe this relation (more on this in Chapter 5). For now, we leave this in its general form. The boundary condition requires knowledge of $\frac{\partial}{\partial x_i}\sigma(\Gamma)$. We note that even with the surfactant-gradient contributions, we can consider the surface stress as the stress tensor evaluated on the surface of the fluid. So, $\frac{\partial}{\partial x}\sigma(\Gamma) = \hat{t} \cdot \mathrm{T} \cdot \hat{n}$. Here $\hat{t}$ $(1,0,0)$ corresponds to the vector that is tangential to the surface in the x-direction and $\hat{n} = (0,0,1)$ is the normal vector to the free surface. Evaluating the tensor product gives us T_{13}. Since this is an off diagonal term of the stress tensor, we know this must be the result of a non-zero strain-rate tensor. So we have

$$\frac{\partial}{\partial x}\sigma(\Gamma) = 2\mu D_{13}.$$

Note that $D_{ij} = 1/2(u_{i,j} + u_{j,i})$ was defined earlier. For the two dimensional flow we are considering, $D_{13} = 1/2(u_{1,3} + u_{3,1})$. Under the lubrication approximation, $u_{3,1} \ll u_{1,3}$ as the motion we are interested in primarily in the $x - y$ plane. This allows us to form the final boundary condition

$$\frac{\partial}{\partial x}\sigma(\Gamma) = \mu u_{1,3}.$$

3.1.6 Integrating the Pressure PDE

Since pressure is a scalar, we can integrate Equation 3.20 applying the boundary conditions described in the previous subsection. Integrating Equation 3.20 results in

$$p = \mu h_{11} - \rho g(h - z) + p_a tm \tag{3.24}$$

This is then differentiated with respect to x to give,

$$p_1 = \mu h_{111} - \rho g h_1. \tag{3.25}$$

Plugging in the relationship with p_x,

$$\mu u_{33} = \mu h_{111} - \rho g h_1. \tag{3.26}$$

By definition, the height h is independent of z, so we can integrate with respect to z and apply the tangential surface stress condition to get

$$\mu u_3 = (\mu h_{111} - \rho g h_1)(h - z) + \sigma_1. \tag{3.27}$$

We integrate once more, but this time we apply the no-slip boundary condition to get

$$\mu u_3 = (\mu h_{111} - \rho g h_1)(hz - \frac{z^2}{2}) + \sigma_1 z. \tag{3.28}$$

3.1.7 Applying Conservation of Mass

The next step is to apply conservation of mass, but to do so we need to define an average velocity. We use a depth-averaged velocity for this purpose

$$\bar{u} = \frac{1}{\mu h} \int_0^h u dz \tag{3.29}$$

Plugging in for u,

$$\bar{u} = \frac{1}{\mu h}\left((\mu h_{111} - \rho g h_1)\frac{h^3}{3} + \sigma_1 \frac{h^2}{2} \right). \tag{3.30}$$

We now use this depth-averaged velocity in the expression for conservation of mass, which is

$$\frac{\partial h}{\partial t} + \frac{\partial (h\bar{u})}{\partial x}. \tag{3.31}$$

Equation 3.31 is a statement of conservation of mass, where we equate the time rate of change of the height to the flux of fluid at that point. Substituting in for the depth-averaged velocity gives us the height equation

$$h_t + \frac{1}{\mu}((\mu h_{111} - \rho g h_1)\frac{h^3}{3} + \sigma_1 \frac{h^2}{2})_1 = 0. \tag{3.32}$$

We then apply conservation of surfactant, equating the flux of the surfactant with the time rate of change, adding on an ad-hoc diffusion term. We assume here that the surfactant is transported at the bulk velocity. Conservation of surfactant with diffusion gives us the following relation

$$\Gamma_t + (\Gamma \bar{u})_1 = D\Gamma_{11}. \tag{3.33}$$

where D is a diffusion constant. Substituting in for $\bar{u}$ gives us the surfactant equation

$$\Gamma_t + \frac{1}{\mu}((\mu h_{111} - \rho g h_1)\frac{\Gamma h^2}{3} + \sigma_1 \frac{\Gamma h^2}{2})_1 = D\Gamma_{11}. \tag{3.34}$$

Since both the height and the surfactant equations are conservation laws that contain $\bar{u}$, it is not surprising that the terms in both the equations have very similar forms.

3.1.8 The Governing Equations

Finally, we arrive at the two governing equations of this system—one for the evolution of the height of the film, and the second for the evolution of surfactant concentration. Together, they form a coupled system of non-linear, mixed, partial differential equations. The non-dimensionalized form of the system is presented below where h is the height and Γ is the surfactant concentration. Note that we now switch back to vector notation, as that allows us to represent the equations more compactly. The vector notation would also provide greater physical intuition for a mathematical audience.

$$h_t + \nabla \cdot (\frac{1}{2}h^2 \nabla \sigma(\Gamma)) = \beta \nabla \cdot (\frac{1}{3}h^3 \nabla h) - \kappa \nabla \cdot (\frac{1}{3}h^3 \nabla \Delta h) \tag{3.35}$$

$$\Gamma_t + \nabla \cdot (h\Gamma \nabla \sigma(\Gamma)) = \beta \nabla \cdot (\frac{1}{2}h^2 \Gamma \nabla h) - \kappa \nabla \cdot (\frac{1}{2}h^2 \Gamma \nabla \Delta h) + \delta \Delta \Gamma \tag{3.36}$$

The constants in the equations above are defined as follows:

$$\beta = \frac{\rho g H^2}{S} \qquad \kappa = \frac{\gamma H^2}{SL^2} \qquad \delta = \frac{\mu D}{SH}$$

3.1.9 Interpreting the Governing Equations

We consider each term of the height equation and the diffusion term in the surfactant equation. The $h^2\nabla\sigma(\Gamma)$ term represents the influence of the surfactant concentration. $\sigma(\Gamma)$ is the equation of state, and, in our case, it is empirically determined. This term accounts for the effect of the change in surface stress due to the surfactant concentration gradient. If Γ is set to 0, i.e. there is no surfactant, we recover the height equation that describes a thin film. The $h^3\nabla h$ terms arises from applying conservation of mass on the fluid and represents the influence of gravity. Note that constants such as g, the acceleration due to gravity, are clubbed into the constant β. The last term $h^3\nabla\Delta h$ represents capillary forces which would exist whenever the fluid is perturbed (non–uniform height). The constant κ encompasses the capillarity constant. This term represents the intrinsic surface tension of the fluid (surface tension without the surfactant).

The corresponding terms in Equation 3.36 represent the change in surfactant concentration for precisely the same reasons. We assume that the surfactant at the surface is carried along with the fluid when the fluid moves.The three terms which determine the motion of the fluid are also present in Equation 3.35. There is an additional $\Delta\Gamma$ term in Equation 3.36. This is an ad-hoc term which represents diffusion; the surfactant is thus assumed to spread by Fick's Law along in addition to being transported by the bulk.

3.1.10 Initial Conditions

The coupled system described in Equation 3.35 and Equation 3.36, we need initial conditions to complete posing the problem mathematically. As discussed in Chapter 2, we need azimuthally symmetric initial conditions. The two initial conditions we use are inward spreading and outward spreading. For both initial conditions, we divide the spatial domain into two regions: an inner disk and an outer ring. The initial fluid height is uniform in both cases, though the surfactant concentrations differ. In the inward spreading initial condition, we set the surfactant concentration to be high in the annular region and low in the disk. The difference in surface tension will cause the fluid to be pulled into the disk, hence this is called inward spreading. The outward spreading case is the exact opposite where we have a high surfactant concentration in the disk and low surfactant concentration in the annular region. We would expect the fluid to get pulled outward for this initial condition. A radial profile of these two initial conditions are

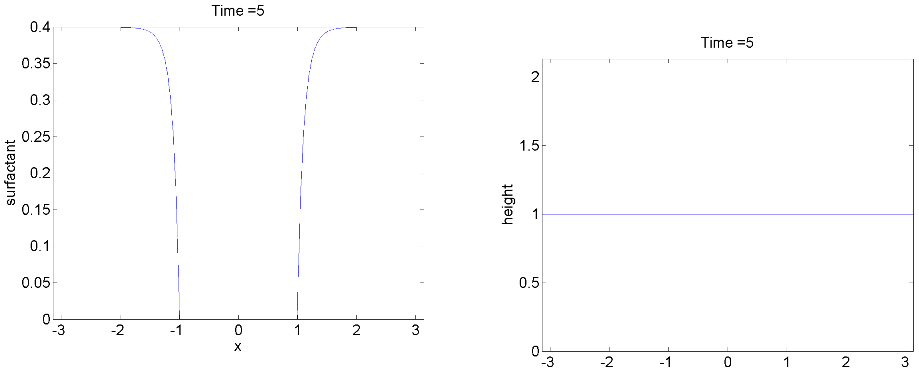

a. The initial condition (surfactant) for inward spreading runs: high surfactant concentration in an annular region with no surfactant concentration in a central disk. This is a radial profile.

b. The initial condition (height) for inward spreading runs: a film of constant height. This is a radial profile

Figure 3.1 Initial conditions used in inward simulations.

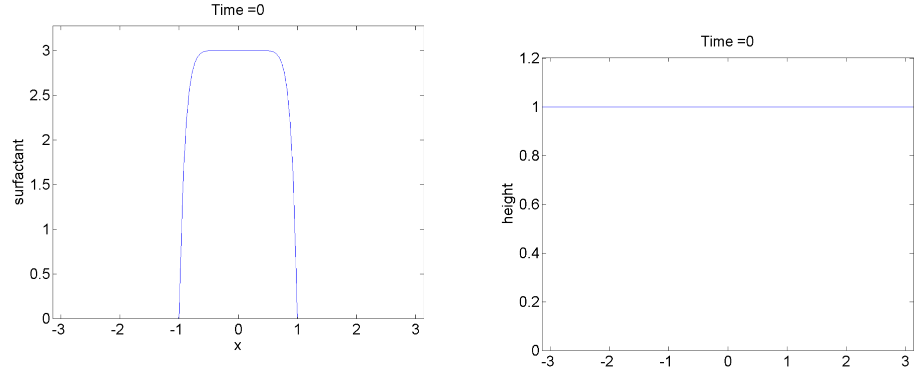

a. The initial condition (surfactant) for outward spreading runs: no surfactant concentration in an annular region with high surfactant concentration in a central disk. This is a radial profile.

b. The initial condition (height) for outward spreading runs: a film of constant height. This is a radial profile.

Figure 3.2 Initial conditions used in outward simulations.

presented in Figures 3.1 and 3.2. The initial condition for the height is constant; for the surfactant though, we define a piece-wise function while using a high degree polynomial (usually a 10th degree polynomial) to create a steep yet non-infinite derivative at the boundary between the high and no surfactant. We should note that the initial conditions we are using are a simplification of the true initial condition in the experiments. This is because the lifting of the ring causes a meniscus to form; the dynamics begin when the meniscus breaks. These initial conditions completely ignore the meniscus.

Chapter 4

Numerics

The governing equations derived in the previous sections are highly non-linear, and hence are challenging to solve numerically. Over the past five years, Jonathan Claridge, Rachel Levy and Jeffrey Wong have developed a software suite that solves fourth-order, non-linear, mixed type systems (Claridge et al., 1990). This is the software we will be using, though there are other options available such as EPDCOL (Craster and Matar, 2006).

4.1 Implicit Solvers by Claridge, Levy and Wong

Implicit Solvers, the suite developed by Claridge, Levy and Wong is an extension to Clawpack, an open-source software that was developed by Randy Leveque's group out of the University of Washington. The numerical computation is performed in Fortran, but there is a Python wrapper that facilitates easy use. Clawpack, which stands for Conservation Law Package, is built to solve systems of PDEs that can be expressed in the form of conservation laws, i.e when one can represent the system in the unknown $\mathbf{u}$ as $\mathbf{u}_t + \nabla \cdot F(\mathbf{u}) = 0$. Expressing a system as a conservation law decouples the spatial and time derivatives, which facilitates numerical solutions. This method restricts the class of PDEs to hyperbolic PDEs. However, the system presented in Equation 3.35 and Equation 3.36 is a mixed type—it consists of hyperbolic terms and parabolic terms. Claridge et al.'s extension solves non-linear, mixed, PDE's by leveraging Clawpack to solve the hyperbolic parts and an implicit method to solve the parabolic parts.

4.1.1 The Mechanics of the Implicit Solver

Most PDE solvers employ three steps to go from a PDE with initial and boundary conditions to the solution—reduce the PDE to an ODE, solve the ODE using an integration scheme, and then recover the solution by solving the system of equations that results from solving the ODE. The mechanics of implicit solvers is explained using this framework.

Converting the PDE into an ODE: The first step is to convert the PDE into an ODE. This essentially involves getting rid of one of the derivatives by approximating them. Implicit Solvers chooses to approximate the spatial derivatives by discretizing the spatial domain into square grids, and then calculating the fluxes into and out of these grid cells. This then converts the PDE into an ODE in time. It is important to note that Implicit Solvers is a finite volume method as opposed to finite difference method. The fluxes (in our case for height and surfactant concentration) are then calculated using user-inputted expressions that are determined by the exact PDE system under consideration.

Integrating the ODE: Claridge et al. employ the Crank-Nicolson scheme for second-order integration to convert the ODE to a system of algebraic equations. The Crank-Nicolson scheme involves the joining of half steps of forward and backward Euler integration. For a function u in one spatial dimension where

$$\frac{\partial u}{\partial t} = F(u, x, t, \frac{\partial u}{\partial x}, \frac{\partial^2 u}{\partial x^2}) \tag{4.1}$$

the Crank-Nicolson method employs the following finite difference

$$\frac{u^{n+1} - u^n}{\Delta t} = \frac{1}{2}[F_i^{n+1} + F_i^{n-1}]. \tag{4.2}$$

where i represents the discretization in space and n represents the discretization in time. This integration scheme is chosen since it is very stable for parabolic terms, which are the terms that Implicit Solvers directly deals with.

Solving the algebraic system: The algebraic system that results from the previous step then needs to be solved to recover the desired function values. If the algebraic system is linear, then BiCGSTAB (Biconjugate gradient Stability) is used to solve the linear system of equations. The choice of BiCGSTAB is fairly arbitrary as other schemes like CGSTAB would have worked too; however, BiCGSTAB does converge quickly to a solution and produces accurate results for our PDE system. With many PDEs, like ours, the integration scheme in the previous step produces a nonlinear system of equations—this is a consequence of the PDEs themselves being nonlinear. In this case, Implicit Solvers then uses continuous space linearization to convert the nonlinear system into a linear system that BiCGSTAB can then solve.

The last important piece of the solver is the implementation of boundary conditions using ghost cells. Essentially, instead of using irregular stencils on the boundary, the program keeps track of the values on 'ghost cells' that are located outside the region of interest. The values for these ghost cells are determined by extrapolating the values of height and surfactant concentration using a cubic polynomial approximation.

Chapter 5

Experimental Factors that Inform the Model

5.1 The Equation of State

An equation of state relates various system variables; examples include pressure, temperature and volume in the ideal gas equation or the stress-strain relation in continuum mechanics. In our case, the equation of state relates the surface tension to the surfactant concentration ($\sigma(\Gamma)$). The incompressible Navier-Stokes equations under the lubrication approximation do not account for the influence of surfactant on the surface stress of the fluid. Without the equation of state, the equations for the time-evolution of the height of the thin film and the surfactant concentration are uncoupled; it is the equation of state that incorporates the surfactant 'driving' the fluid behavior. The equation of state closes the system by providing this missing relation.

5.1.1 Previous Equation of States

Our model requires a monotonically decreasing function for the equation of state since, up to a minimum surface tension, a larger surfactant concentration corresponds to a smaller surface tension. The simplest equation of state we could use, given this constraint, would be a decreasing linear function. Apart from the simple form and physical motivation, a linear equation of state has a constant derivative. This facilitates analytical investigation, as the simple form allows for asymptotic similarity solutions (Jensen, 1994). Though Jensen (1994), (Gaver and Grotberg, 1990), and oth-

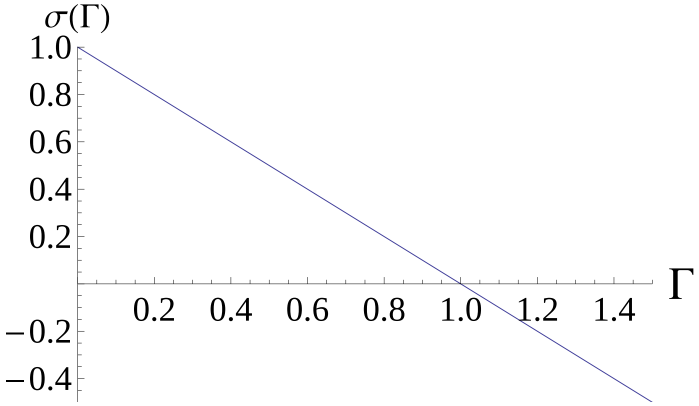

Figure 5.1 The linear equation of state

ers have used a linear relation, a critical issue with a linear relation is that with enough surfactant, one could achieve a negative stress as seen in Figure 5.1 (for a surfactant concentration greater than 1) . This does not conform to the physical limitations of the system. The stress can never become negative, and should instead approach some minimum stress level. One way to model this is to have a decreasing function that asymptotically approaches the minimum stress level; this minimum stress would be empirically determined. This approach motivated multilayer equation of state. The multilayer equation of state (in blue in Figure 5.2) takes on the form $\sigma(\Gamma) = \frac{1}{(1+a\Gamma)^3}$ and can be tuned to asymptotically approach a minimum stress level using the parameter a.

However, the multilayer equation of state is independent of the surfactant used; it ignores the specific chemical properties of individual surfactants. Hence, the next step was to consider if NBD-PC, the specific surfactant our experiments employed had a different equation of state. A review of the literature revealed that Tsukanova et al. (2002) had in fact collected data which indicated that the relation resembles a hyperbolic tangent. Stephen Strickland from NC State then collected more data at the Daniels Lab at NC State to reaffirm this finding. This data has prompted us to compare the simulation results generated using the empirical equation of state with experimental observations.

It is important to note that even though Strickland's data suggests to a hyperbolic tangent equation of state, it is not guaranteed that the surfactant in our experiments will behave in the same manner. Strickland's data was collected in a Langmuir trough, an apparatus that has a rectangular

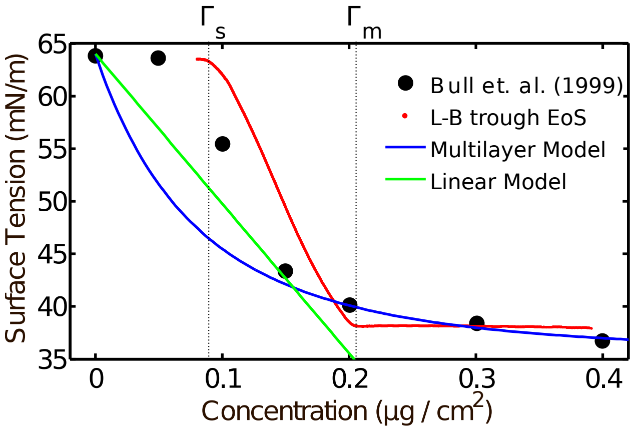

Figure 5.2 Different Equations of State with Stephen Strickland's data in red.

geometry with a thick film. A Langmuir trough compresses the molecules on the surface of a fluid, and measures the resistance to this compression. It involves a cuboidal bath with a movable plate that compresses the top layer of the fluid. A pressure sensor records the resistance the plate encounters thereby measuring the surface pressure. The surface pressure is in some ways the inverse of surface tension: surface pressure $= \Gamma_0 -$ surface tension of a fluid which has surfactant (where Γ_0 is the free surface tension of the fluid, i.e the surface tension when no surfactant is present). We expect this intrinsic surface tension to be the maximum surface tension of the fluid. As we start adding surfactant, the surface tension reduces, causing the surface pressure to increase. A good analogy is that of a rubber sheet—when stretched taught, it is under maximum tension. If we subject it to a tangential compressive force (against the tension), the sheet looses its tautness thereby reducing tension. The surface pressure is analogous to the compressive force applied to fold the rubber sheet.

5.1.2 Impact of the EoS

Since one of the primary aims of this thesis is to compare the results produced by the multilayer and the empirical EoS, it is worth considering exactly how the EoS plays into the system. As we saw in Chapter 3, the governing equations for both surfactant and height contain a $\nabla\sigma(\Gamma)$ term. Thus it is not the EoS itself, but rather its gradient that influences the height and surfactant profiles. Expanding the gradient using the chain rule, we see that

$$\nabla\sigma(\Gamma) = \frac{d\sigma(\Gamma)}{d\Gamma}\nabla\Gamma. \tag{5.1}$$

Thus, there are two important pieces—first, the shape of the derivative of the EoS (with respect to Γ) and the surfactant concentration gradient at the given point. Based on this understanding, we can identify a couple of important differences between the multilayer and empirical EoS. These two EoS, along with their derivatives are plotted in Figures 5.3a and 5.3b respectively.

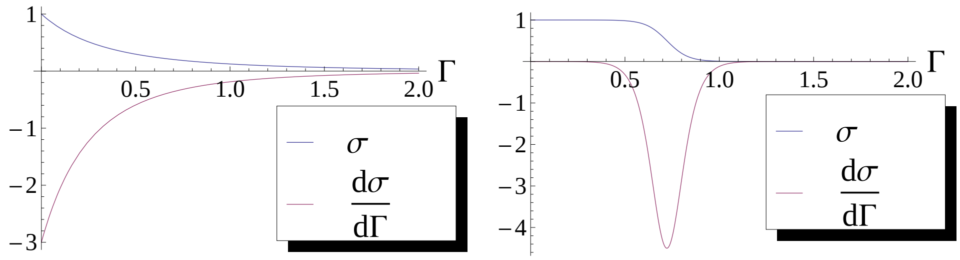

a. The multilayer EoS and its derivative. The derivative increases in magnitude as the concentration reduces.

b. The empirical EoS and its derivative. The derivative is non-zero for a very small portion (in this case between concentrations of 0.6 and 1).

Figure 5.3 The multilayer and empirical EoS with their derivatives. Note that the exact values are not the same as those used in the simulations, though the general shape is the same.

As we see in in Figure 5.3a and Figure 5.3b, the difference in the functional forms cause a marked difference in the derivatives. The multilayer equation of state has maximum derivative at low surfactant concentrations. Thus, the lower the surfactant concentration, the greater the influence of this term. On the other hand, the empirical EoS has a near zero derivative for the majority of the concentration domain. Thus, it is only in the narrow band between about 0.6 and 1 (in Figure 5.3b) that the EoS even influences the dynamics. Consequently, unlike with the multilayer EoS, for very high and very low surfactant concentrations, we expect the surfactant motion to be governed by diffusion, while there would be rapid dynamics when in the narrow region non-zero region of the derivative.

In order to aid interpreting of results in Chapter 6, we divide the empirical EoS into 3 regions—A, B and C based on whether the derivative is non-zero—this division is presented in Figure 5.4. We can then consider the

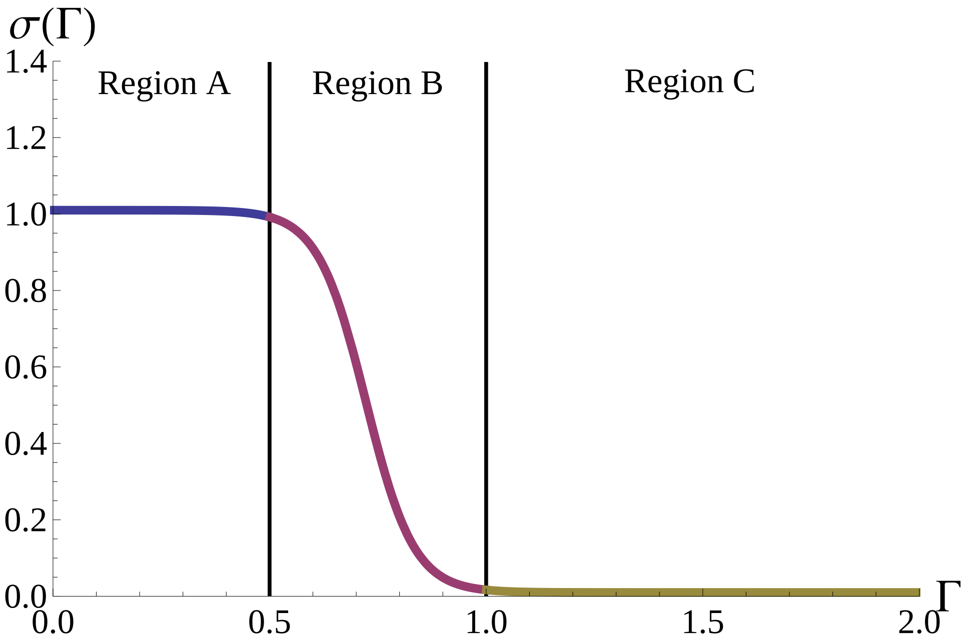

Figure 5.4 The empirical EoS can be divided into three regions based on the value of its derivative (whether the derivative is non-zero or not). This division will be referred to in Section 6 to interpret the simulated profiles.

surfactant concentration dynamics in relation to these three regions. Interestingly, we see that the choice of representation of the empirical EoS will significantly affect our results.For example, if we had chosen a piece-wise linear relationship, the derivative, and hence the results would likely be different than those produced with a tanh EoS.

5.2 Nondimensionalizing the Equations

Dimensionless quantities are preferred when numerically solving DEs as the output are easier to interpret. Usually, characteristic quantities are used to scale the dimensional quantities, thus rendering the results as some fraction of the characteristic quantity. For the surfactant spreading experiments the following characteristic quantities are used in this process (these quantities are specific to our experiment, and would vary for different setups).

In addition to the characteristic quantities listed in Table 5.1, we also use a few other material constants. These help non-dimensionalize other

Dimensional Quantity	Char. qty	Description
height—$h(\mathbf{r}, t)$	H	Initial fluid height
spatial coordinate—$\mathbf{r}$	L	Ring radius
surfactant concentration—Γ	Γ_c	Critical micelle concentration
surface tension - σ	S	Surface tension range (max–min)

Table 5.1 Characteristic quantities

dimensional constants that exist in the equations. This allows to define

Constant	Description
ν	Viscosity of fluid
g	Acceleration due to gravity
D	Diffusivity constant of the fluid
σ_0	Surface tension of surfactant-free fluid
ρ	Fluid density

Table 5.2 Fluid and environmental parameters

the scaling for time $T = \frac{\nu L^2}{SH}$, and the following constants $\beta = \frac{\rho g H^2}{S}$, the capillarity constant, $\kappa = \frac{\sigma_0 H^2}{SL^2}$ and the Peclet number, $\delta = \frac{\nu D}{SH}$. In addition, we require a few fluid-specific constants. The simulations presented in this thesis correspond to simulations on glycerol; thus the pertinent parameters of glycerol are listed in Table 5.3.

Variable	Value	Variable	Value
H	1–2 mm	g	9.8 m s^{-2}
L	3 cm	D	10^{-4} cm^2/s
Γ_c	0.2 mg/cm^2	σ_0	64 mN/m
S	27 mN/m	ρ	1.26 g/cm^3
ν	0.950 Pa s	β	0.950 Pa s
κ	0.01	-	-

Table 5.3 Numerical values used for glycerol simulations

5.2.1 Non-dimensionalizing the New Equation of State

The next step is to non-dimensionalize experimentally measured equation of state. The surface tension will be non-dimensionalized using the range of possible surface tension as defined by the EoS. The *tanh* approximation provides a nice way to define the max and the min (as the limits at $\pm\infty$ of the approximation). The surfactant concentration is non-dimensionalized by using the critical micelle concentration as the characteristic concentration. In order to do this quantitatively, we need to perform a curve fit on the measured data. I used Igor Pro, a software that employs non-linear least squares to create best fit functions for data. At this point, it is worth considering the choice of a hyperbolic tangent as the functional form for the equation of state. We could have used any other functional form that resembled a step function such as a sigmoid. We found, however, that the fits created were more or less identical with next to identical residuals. The χ^2 or 'goodness of fit measure was also basically the same (though not very good because of the sharp turn at a surfactant concentration of about 0.2. Since our group had previously worked with the tanh form, we just stuck with it. The tanh and a sample sigmoid fit are presented in Figure 5.5a and Figure 5.5b respectively.

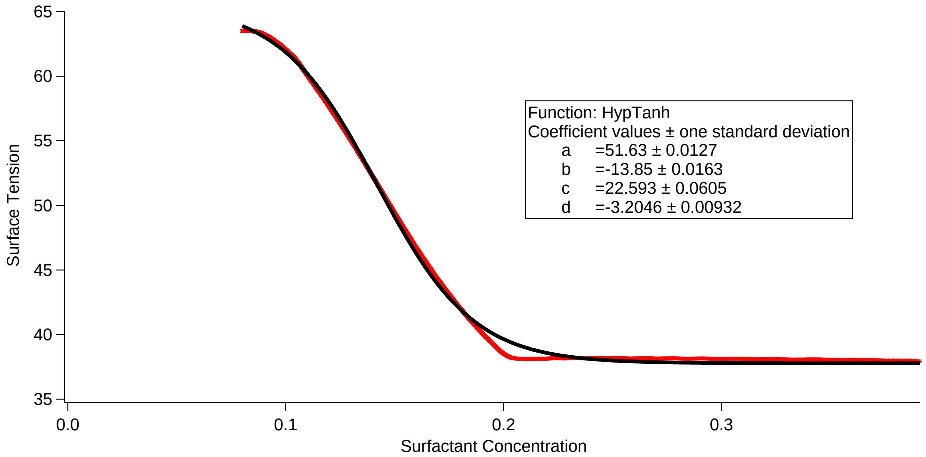

a. Fitting a tanh functional form to EoS data collected at the Daniels Nonlinear Lab at NCSU. The fit is in black with the data in red.

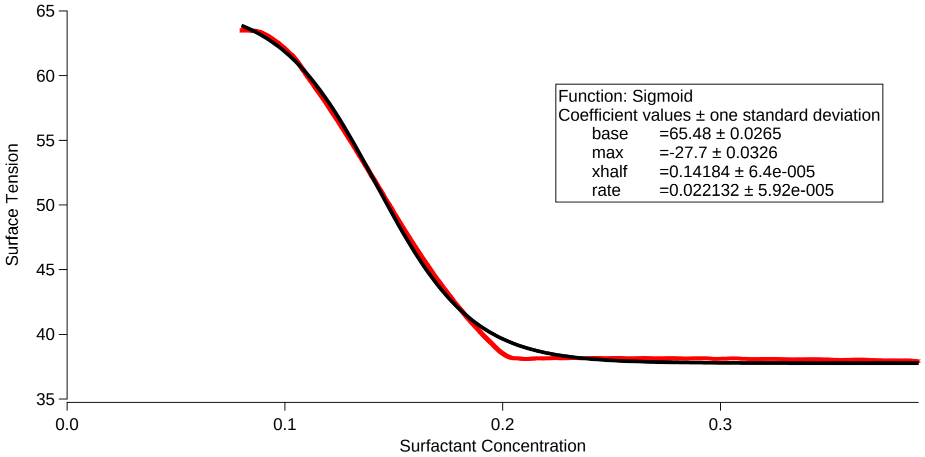

b. Fitting a sigmoid functional form to EoS data collected at the Daniels Nonlinear Lab at NCSU. The fit is in black with the data in red.

Figure 5.5 Fitting a functional form to experimental data collected at NCSU. Note the similarity in the fits and residuals.

Chapter 6

Simulation Results

6.1 Investigating the Impact of the EoS

As stated in Section 5, we are trying to improve the agreement of the simulations with experiment by using an empirical equation of state. In addition to this goal, we are also looking to study the mathematical impact of the empirical equation of state (tanh functional form) on the solutions to the PDE system described in Equations 3.35 and 3.36.

6.1.1 Sanity Checks

Before making these comparisons however, we need to make a few cursory checks regarding the output of the simulations: we need to verify that the numerical solutions to our model are also azimuthally symmetric (just like in the experiments) and that our pde solver conserves mass and surfactant

Verifying Azimuthal Symmetry of the Solutions

The azimuthal symmetry of the solutions is an interesting feature. It is important to note that we do not explicitly enforce azimuthal symmetry, the solutions 'just happen' to be azimuthally symmetric. Apart from the intuition that we gain from the experimental data, a physical argument also supports azimuthally symmetric solutions. Given an azimuthally symmetric initial condition, there is no reason for the forces described by Navier-Stokes equations and the surfactant concentration gradient stresses to favor one direction over another. However, if we were to add random noise to our initial condition, we would obtain fingering. Since our experiments do not show fingering (at least on the length scales that we can detect and are

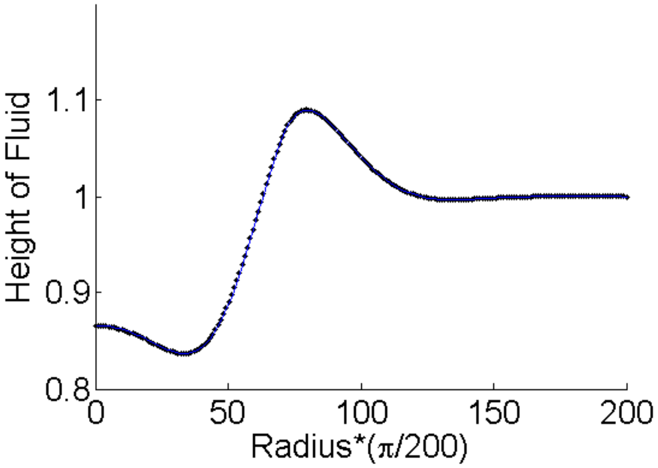

Figure 6.1 A slice at $\theta = 0$ of the height profile in blue with the azimuthally averaged profile in black. We see perfect agreement.

interested in), we do not add noise to our initial conditions. A radial slice of out solution at $\theta = 0$ along with the azimuthally averaged solution is presented in Figure 6.1. Note that the dotted line and the curve agree very well.

Verifying conservation of mass and surfactant

An important part of the derivation of the model involves using conservation of mass and by extension conservation of surfactant. Hence, to verify if the numerical results are faithful to the model, we need to make sure that the output is indeed conservering mass and surfactant. To do this we integrate the area under the height and surfactant profiles using an approximate integration scheme (trapezoidal method) at different times. Plots of the respective areas (which correspond to the total fluid and the total surfactant) over time for an outward spreading run are presented in Figures 6.2a and 6.2b. Since these plots are derived from the azimuthally averaged profiles, when we integrate, we need to make sure that the values at larger radius are weighted more (by a factor of $2\pi r$). Note that while the lines look very flat, there is some slight variation on the order of 10^{-1} and 10^{-3} for the fluid and surfactant respectively, which is due to the numerical error given our gridsize of about 0.03. The height profile shows a minor increase at about t = 1.6 second, we believe this is negligible.

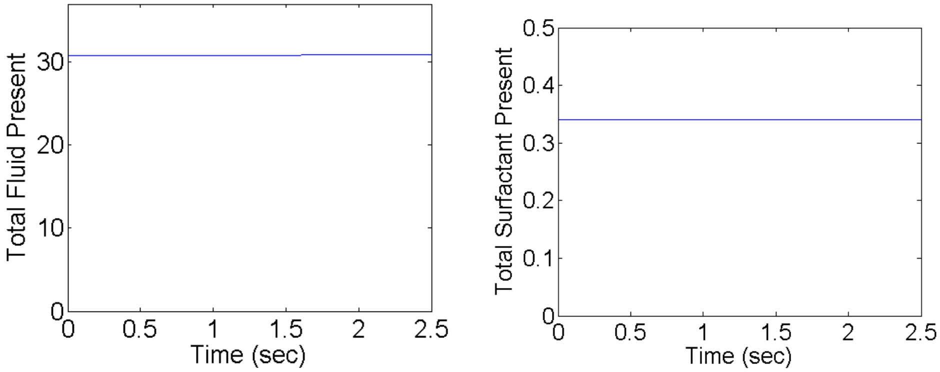

a. The total (integrated) fluid over time for an outward spreading run. The initial surfactant concentration was 0.13 Γ_c. Note that the line is very flat; there are however fluctuations on the order of $10^{-1}m$ due to numerical error.

b. The total (integrated) surfactant over time for an outward spreading run. The initial surfactant concentration was 0.13 Γ_c. Note that the line is very flat; there are however fluctuations on the order of $10^{-3}m$ due to numerical error.

Figure 6.2 Verifying conservation of mass and surfactant

6.1.2 Comparing the Multilayer and the Empirical EoS

We now want to compare the performance of the multilayer equation of state to the empirical equation of state. We make both qualitative and quantitative comparisons. The qualitative comparisons involve making key observations regarding the similarities and the differences between the results using the two EoSs. The quantitative comparisons involve extracting key statistics which are easy to contrast against experimental data.

In all most of the following figures (unless otherwise noted), we use a spatial domain of $x \in [-2\pi, 2\pi]$ and $y \in [-2\pi, 2\pi]$. We use 500 grid points in both the x and y directions giving us a grid cell of size 0.06. We also run our simulations for around 5 seconds for inward spreading runs and 2.5 seconds outward spreading runs. The reason I did not run them for longer is that a single simulation for one of these takes 36 hours. We had to compromise the length of simulations against the number of data points and ability to look at our results.

6.1.3 Quantitative Comparisons

While the influence of the change in functional form of the equation of state on the results is mathematically interesting, the ultimate purpose of this investigation is to bring the simulation results closer to the experimental observations. A good way to compare the two is to identify key statistics that can be easily extracted from both the simulation and experimental data. These statistics or characteristics can also provide reasonable quantitative comparisons between the two equations of state. The following list are possible characteristics we might wish to extract. In this thesis, we focus on the height at the center and the leading edge of the surfactant.

- Marangoni ridge: There are three important characteristics associated with the Marangoni ridge—the height of the ridge, the position of the ridge and the spreading rate of the ridge (velocity of the ridge).
- Leading edge of surfactant: There are two important characteristics associated with the leading edge—again the position of th edge, and the spreading rate.
- Statistics related to the center: This is especially relevant to the inward spreading runs thought outward spreading has also lead to interesting behavior at the center. Here we are just looking at the height and surfactant concentrations at the center over time.
- The anular trough in the wake of the wave is also another interesting feature; this can be viewed as a complement of the Marangoni ridge that arises since mass is conserved. We would be interested in the depth, position of the lowest point, and possibly the width of the trough.

6.1.4 Inward Spreading Simulations

The surfactant and height profiles using the multilayer equation of state and the empirical equation of state are presented in Figures 6.3 and 6.5.

Surfactant Profiles

We begin with a discussion of the surfactant profiles, as the surfactant behavior informs the height profiles. There are important qualitative differences in the evolution of the surfactant with respect to the two equations of state.

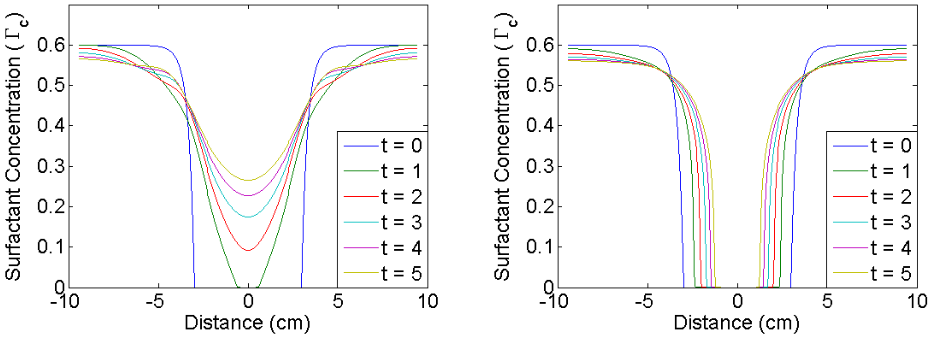

a. The surfactant profiles of an inward spreading run starting with $\Gamma_0 = 0.6\Gamma_c$ at times t = 0, 1, 2, 3, 4 and 5 seconds using the multilayer EoS. We see that the surfactant 'closes the hole' faster while the surfactant gradient becomes shallow.

b. The surfactant profiles of an inward spreading run starting with $\Gamma_0 = 0.6\Gamma_c$ at times t = 0, 1, 2, 3, 4 and 5 seconds using the empirical EoS. The steep surfactant gradient from the initial condition is maintained while the hole takes longer to close much longer to close (more than 10 seconds).

Figure 6.3 Surfactant profiles for the multilayer and empirical EoS at 0.6 Γ_c.

First, we note that there is a difference in the general shape of the profiles. The multilayer equation of state smoothens the steep gradient in the surfactant initial condition very quickly, leading to a a gentle slope in the surfactant 'hole'. The empirical EoS on the other hand maintains the steep gradient even at relatively late times. Next, we see that the multilayer EoS closes the hole in less than 2 seconds while this does not occur with the empirical EoS. The empirical EoS thus appears to lead to slower dynamics (at least at initial concentrations of around 0.6 Γ_c).

The difference in shapes can be explained, to a large extent, by the different functional forms of the two EoSs. The multilayer EoS has the largest derivative for the low amounts of surfactant; consequently, we see the surfactant at low concentrations spread inward faster. Also, we note that once the hole is closed, it takes a long tome for it to fill out. One reason for this is that the surfactant concentration has a local minimum at $r = 0$ after hole closure. The local minimum implies that $\nabla\Gamma = 0$. Furthermore as the surfactant concentration increases (by diffusion or otherwise), $\frac{\partial\sigma}{\partial\Gamma}$ reduces due to the decreasing nature of the multilayer EoS. On the other hand, with the empirical EoS, $\frac{\partial\sigma}{\partial\Gamma}$ is basically 0 for surfactant concentrations less than $0.6\Gamma_c$. Consequently, we see the surfactant 'creeping' inward in the case of the

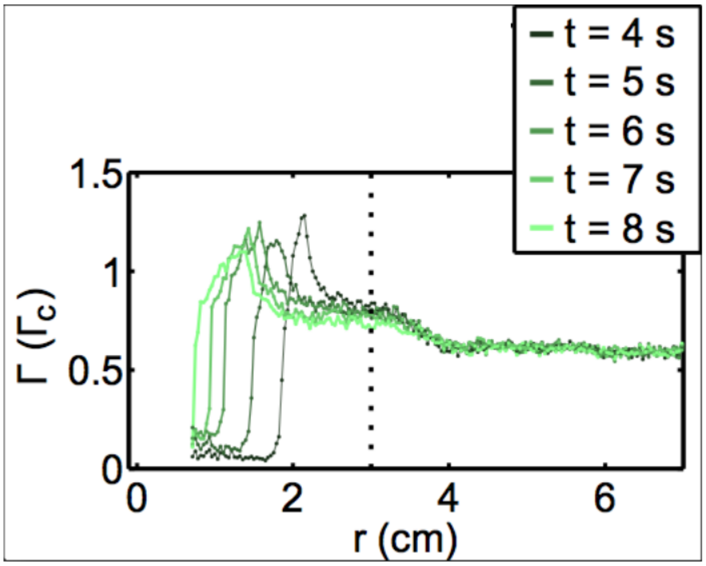

Figure 6.4 Surfactant profiles from experimental runs carried out at the Daniels Non-Linear Lab at NCSU. We see steep surfactant gradients similar to those produced by the empirical EoS. Strickland et al. (2014)

empirical EoS, leading to slower dynamics.

We note that the preserving of the steep gradient of surfactant concentration at the leading edge is a very promising sign for the empirical EoS. Inward spreading experimental runs have yielded surfactant profiles where a steep gradient is preserved as the leading edge moves inward. This feature is clearly absent in the profiles created using the multilayer EoS. We see surfactant profile data extracted at NC State Lab in Figure 6.4 where the gradient is preserved Strickland et al. (2014). However, we see that the experimental profiles have an inward spreading peak of surfactant, while our profiles are monontonically increasing with increasing r. It is possible that this feature is due to meniscus effects caused by the lifting of the ring (we are running simulations on this and should have some preliminary results soon), but this could also be indicative of the model not capturing an important feature in the surfactant profile.

Height Profiles

The differences in the height profiles mirror those of the surfactant profiles. There are two major differences—the time scale of dynamics is slower in

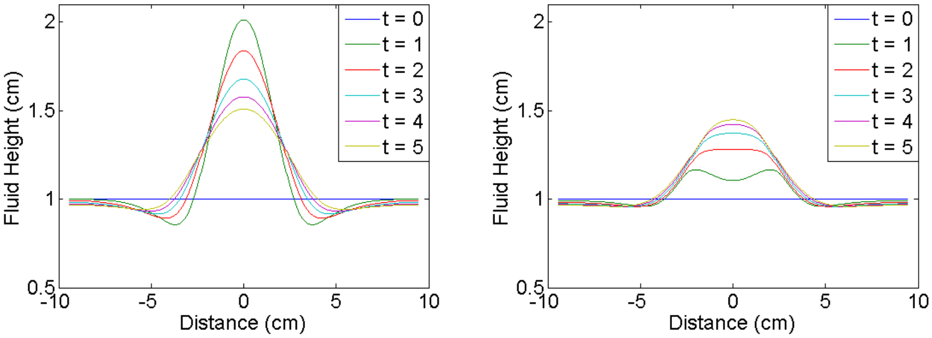

a. The height profiles of an inward spreading run starting with $\Gamma_0 = 0.6\Gamma_c$ at times t = 0, 1, 2, 3, 4 and 5 seconds using the multilayer EoS. We see that the central distension (and Marangoni ridge) is larger while the distension also forms faster.

b. The height profiles of an inward spreading run starting with $\Gamma_0 = 0.6\Gamma_c$ at times t = 0, 1, 2, 3, 4 and 5 seconds using the empirical EoS. The central distension is smaller while the time scale of dynamics is slower.

Figure 6.5 Height profiles for the multilayer and empirical EoS at 0.6 Γ_c.

the case of the empirical EoS compared to the multilayer EoS. Since the surfactant profiles drive the height profiles, this difference in time scales is a consequence of a similar time scale difference in the surfactant profiles. Next, we see that the height of the central distension is also different—the multilayer EoS leads to a larger central distension. The cause of this can again be tied back to the shapes of the respective equations of state. The region of zero-stress in the middle causes the marangoni forces to be considerably smaller with the empirical EoS, while the opposite is true with the multilayer EoS—the central region has the largest force as $\frac{d\sigma(\Gamma)}{d\Gamma}$ is larger for smaller surfactant concentrations.

Our analysis of the difference in results produced by the two relations hinges on the fact that a lot of the dynamics with $\Gamma_0 = 0.6\Gamma_c$ is governed by the flat region of the empirical EoS (region A) (while 0.6 itself is near the boundary, the majority of the profile moves into region A at very short times). Hence, if we were to increase the initial surfactant concentration, so a larger proportion of the domain was in region B of the empirical EoS, we would expect the results to be different. Hence, we try $\Gamma_0 = 0.8\Gamma_c$, which is in the middle of region B. The surfactant and height profiles for $\Gamma_0 = 0.8\Gamma_c$ are presented in Figures 6.6 and 6.7.

As the EoS analysis suggests, the surfactant hole now closes at a similar rates with both equations of state, though the shape of the profiles are

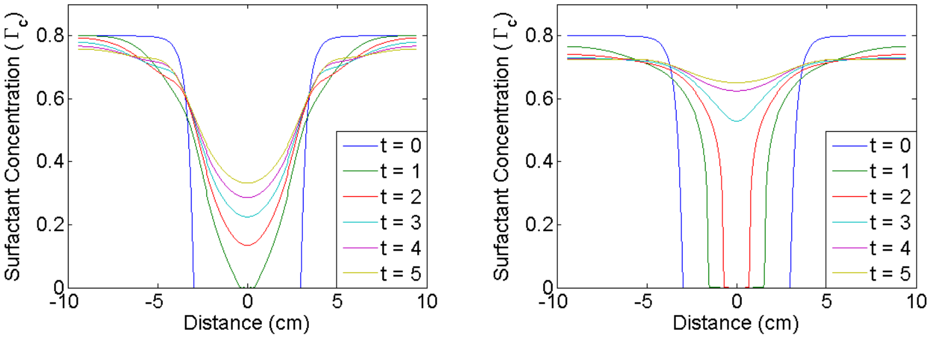

a. The surfactant profiles of an inward spreading run starting with $\Gamma_0 = 0.8\Gamma_c$ at times t = 0, 1, 2, 3, 4 and 5 seconds using the multilayer EoS. The dynamics do not differ much from the $0.6\Gamma_c$ case.

b. The surfactant profiles of an inward spreading run starting with $\Gamma_0 = 0.8\Gamma_c$ at times t = 0, 1, 2, 3, 4 and 5 seconds using the empirical EoS. While the shape of the profiles is similar, starting in region B of the EoS speeds up the time scale of the dynamics tremendously.

Figure 6.6 Surfactant profiles for the multilayer and empirical EoS with $\Gamma_0 = 0.8\Gamma_c$.

different as discussed above. Interestingly the height profiles produced by the empirical EoS are still slower than the multilayer EoS. This differential behavior is likely since as seen in Equation 3.36, the EoS influences the surfactant profile through $\Gamma\nabla\sigma(\Gamma)$ term as opposed to just a $\nabla\sigma(\Gamma)$ term in the height profiles. One possibility is that the presence of the extra Γ causes the surfactant dynamics to speed up, while not affecting the height dynamics; however we need to study this further.

Regime Hypothesis

Based on the functional forms of the multilayer and empirical EoS, a key difference we have identified is that the empirical EoS has three distinct regions where we expect qualitatively different behavior, as opposed to the multilayer EoS, where no distinct regions exist. Thus, we expect a significant 'jump' or transition in results as the initial surfactant concentration moves from region A to region B, while such a transition would not be expected in the case of the multilayer EoS. In fact this is exactly what we see—such a transition exists somewhere in between 0.6 and 0.8 Γ_c as seen in the surfactant concentration plots in Figure 6.8. Furthermore, such a transi-

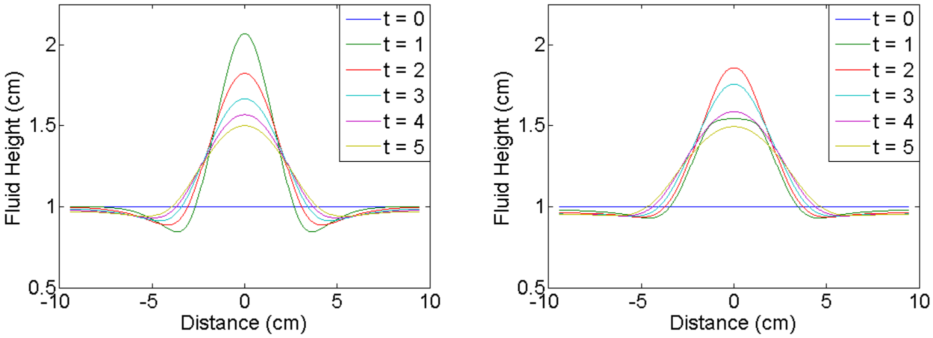

a. The height profiles of an inward spreading run starting with $\Gamma_0 = 0.8\Gamma_c$ at times t = 0, 1, 2, 3, 4 and 5 seconds using the multilayer EoS. The dynamics do not differ much from the $0.6\Gamma_c$ case. The profiles are qualitatively similar to those produced by the empirical EoS, though the time scale is faster with the multilayer EoS.

b. The height profiles of an inward spreading run starting with $\Gamma_0 = 0.8\Gamma_c$ at times t = 0, 1, 2, 3, 4 and 5 seconds using the empirical EoS. While the shape of the profiles is similar, starting in region B of the EoS does not seem to change the height dynamics too much—the height profile is still far behind that of the multilayer EoS.

Figure 6.7 Height profiles for the multilayer and empirical EoS with $\Gamma_0 = 0.8\Gamma_c$.

tion does not exist in the multilayer EoS, as evidenced by the corresponding plot in Figure 6.9. There is preliminary evidence seen by Strickland et al. (Strickland et al., 2014) which suggests that such a transition might occur in the experiments as well, but this needs to be investigated further.

A significant issue with the simulations identified by Strickland et al. is that the simulations occur on a much slower time scale than the experiments. The use of the new EoS does not appear to fix that issue, especially when we are in region A, as the empirical EoS either slows down the dynamics or seems to produce dynamics that occur on a comparable time scale. The time scale discrepancy might point to some deeper flaw in the model, though it could point to an error in the non-dimensionalization as well.

Spreading Rate of Surfactant

A reasonable next step is to consider the spreading rate of the surfactant. Jensen, when he first derived this model, identified an asymptotic spreading rate of the surfactant using self-similarity solutions. He identified the

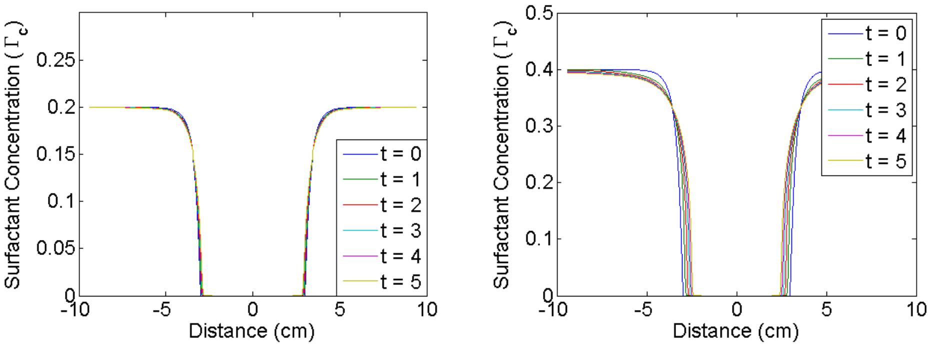

a. The surfactant profiles of an inward spreading run starting with $\Gamma_0 = 0.2\Gamma_c$ at times t = 0, 1, 2, 3, 4 and 5 seconds using the empirical EoS. Dynamics are very slow, primarily governed by diffusion as we are in region A.

b. The surfactant profiles of an inward spreading run starting with $\Gamma_0 = 0.4\Gamma_c$ at times t = 0, 1, 2, 3, 4 and 5 seconds using the empirical EoS. Dynamics are very slow, primarily governed by diffusion as we are in region A.

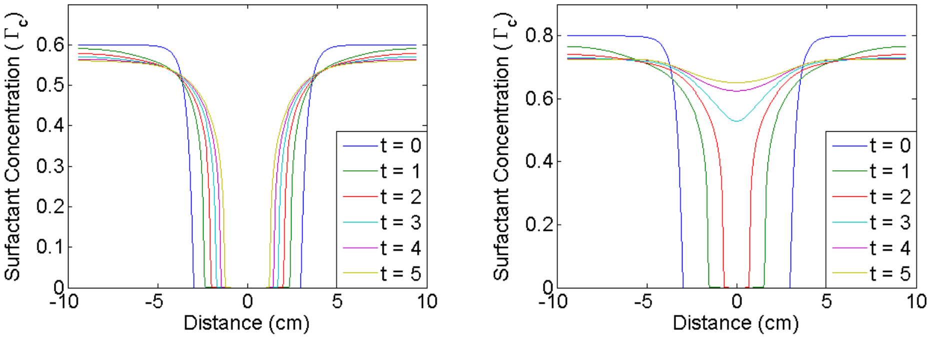

c. The surfactant profiles of an inward spreading run starting with $\Gamma_0 = 0.6\Gamma_c$ at times t = 0, 1, 2, 3, 4 and 5 seconds using the empirical EoS. Dynamics are a little faster at early times but slow down quickly—as we fall back into region A from region B.

d. The surfactant profiles of an inward spreading run starting with $\Gamma_0 = 0.8\Gamma_c$ at times t = 0, 1, 2, 3, 4 and 5 seconds using the empirical EoS. Dynamics are fast, comparable to that of the multilayer EoS—we are in region B.

Figure 6.8 The surfactant profiles at different Γ_0 for empirical EoS.

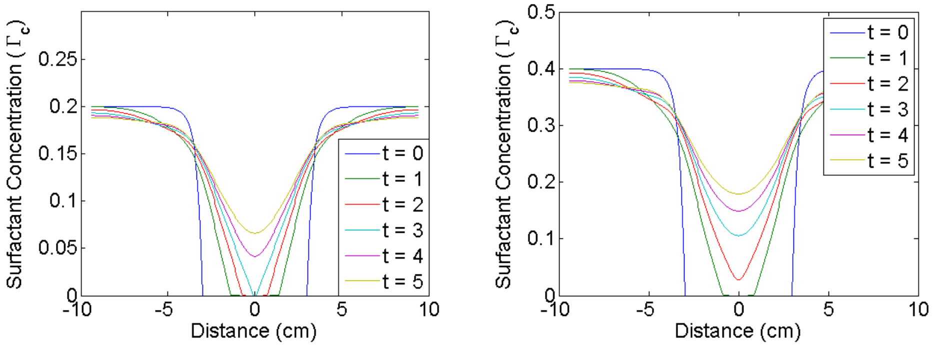

a. The surfactant profiles of an inward spreading run starting with $\Gamma_0 = 0.2\Gamma_c$ at times t = 0, 1, 2, 3, 4 and 5 seconds using the multilayer EoS.

b. The surfactant profiles of an inward spreading run starting with $\Gamma_0 = 0.4\Gamma_c$ at times t = 0, 1, 2, 3, 4 and 5 seconds using the multilayer EoS.

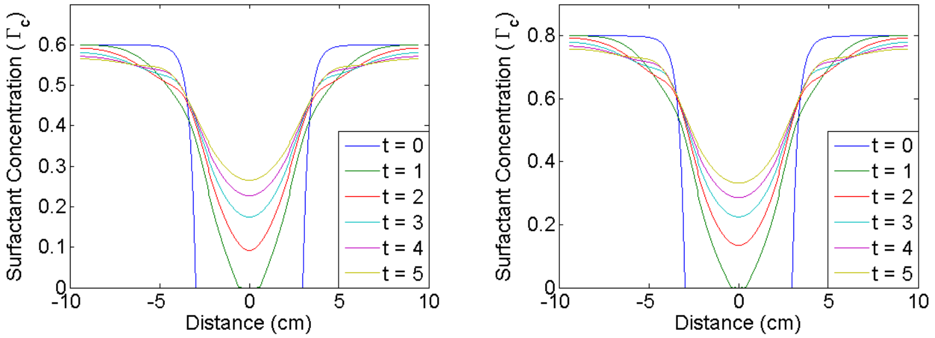

c. The surfactant profiles of an inward spreading run starting with $\Gamma_0 = 0.6\Gamma_c$ at times t = 0, 1, 2, 3, 4 and 5 seconds using the multilayer EoS.

d. The surfactant profiles of an inward spreading run starting with $\Gamma_0 = 0.8\Gamma_c$ at times t = 0, 1, 2, 3, 4 and 5 seconds using the multilayer EoS.

Figure 6.9 The surfactant profiles at different Γ_0 for multilayer EoS. The dynamics hasten as Γ_0 increases but in a uniform way. There is no transition to a different regime.

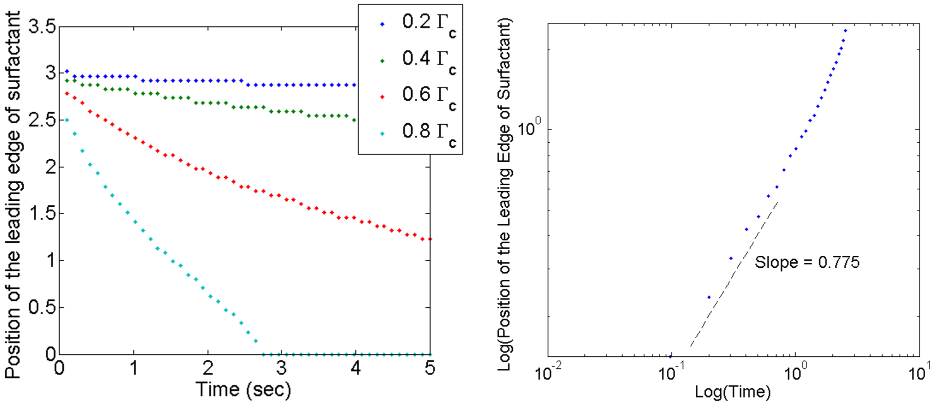

a. The position of the leading edge against time for for Γ_0 = 0.2, 0.4, 0.6 and $0.8\Gamma_c$. We see reaffirmation of different behavior at low and high Γ_0.

b. Log log plot of the leading edge of the surfactant against time for $\Gamma_0 = 0.8\Gamma_c$. We fit r_s against $t - t_c$, where t_c is the time the surfactant hole closes. The slope of 0.775 agrees with theoretical and experimental estimates.

Figure 6.10 Analyzing the leading edge of the surfactant in inward spreading runs using the empirical EoS.

asymptotic spreading rate in terms of t_h the time when the surfactant hole closes. Jensen's prediction was that (Jensen, 1994)

$$r_s \propto (t_h - t)^{0.8} \tag{6.1}$$

Strickland et al. found that simulations produced using the multilayer EoS had a spreading rate of close to 0.8 while experimental data also suggested a similar rate (the experimental data was reliable for only 0.6 and 0.8 Γ_c)Strickland et al. (2014). Consequently, we identify how the spreading rate using the empirical EoS compares [1]. In Figure 6.10a, we see the position of the leading edge of the surfactant against time. Note that this plot also suggests that 0.2 and 0.4 Γ_c operate in a different regime than the $0.8\Gamma_c$ run. Unfortunately, since these simulations take 36 hours, time constraints did not allow us to run these for longer. We only simulate up to hole closure in the $0.8\Gamma_c$ case. In Figure 6.10b we see a log log plot of $(t_h - t)$ versus the position of the leading edge (t_h was identified to be about 2.75 seconds). If we ignore the initial transience, we see that the slope is about 0.775, which is pretty close to Jensen's estimate of 0.8. Thus any difference in the speed with which the surfactant moves (in regime B) between the empirical and multilayer EoS must be due to the proportionality constant rather than the exponent. Since Strickland et al found that experimental evidence suggested a spreading rate of around 0.8, it is good that the empirical EoS retains this important characteristic.

---

[1] Due to the presence of the diffusion term $D\Gamma_{xx}$, mathematically there is no leading edge—the diffusion term ensures that there is non-zero surfactant concentration for all space and for all $t > 0$. However, due to numerical precision, the surfactant concentration does not instantaneously become non-zero for all space. Hence we use the position of the first instance where the surfactant concentration is greater than 10^{-3} to denote the leading edge.

Rate of Distension Decay

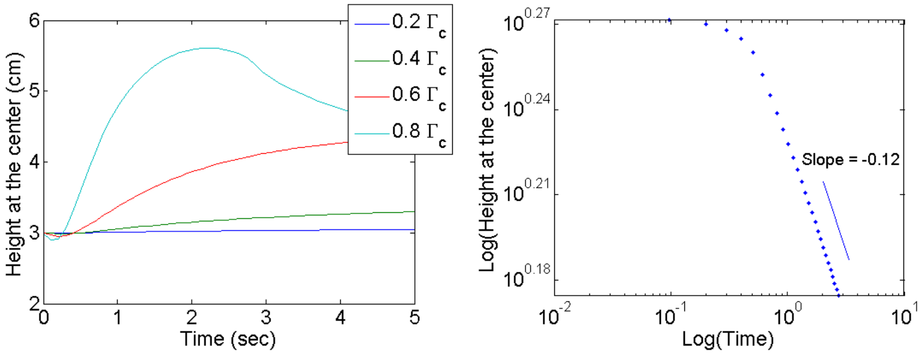

a. The height of the central distension versus time for for Γ_0 = 0.2, 0.4, 0.6 and $0.8\Gamma_c$. We see reaffirmation of different behavior at low and high Γ_0.

b. Log log plot of the leading edge of the surfactant against time for $\Gamma_0 = 0.8\Gamma_c$. We fit h_c against $t - t_m$, where t_m is the time the surfactant hole closes. The slope of -0.12 leads to a slower relaxation than seen in the simulations produced using the multilayer EoS.

Figure 6.11 Analyzing the height of the central distension in inward spreading runs using the empirical EoS.

Another important characteristic of inward spreading surfactant flow is the rate at which the central distension decays, i.e. the evolution of the height at the center after the distension reaches maximum height. There are no theoretical predictions for the rate of distension decay. However, Strickland et al. found that the multilayer EoS led to a rate of distension decay of about $\alpha = -0.33$ where

$$h_c = (t - t_m)^{\alpha} \tag{6.2}$$

and t_m is the time at which the distension reaches maximum height Strickland et al. (2014). Furthermore, Strickland et al. found preliminary experimental evidence to support this rate of decay. We repeat this calculation for profiles produced by the empirical EoS. Again, like with the spreading rate of the surfactant, the distension reaches maximum height only for $0.8\Gamma_c$ in the time we simulated for; hence we can only calculate this rate for one value. This rate was calculated to be -0.12 for $\Gamma_0 = 0.8\Gamma_c$. While this seems to disagree with the experimental data collected by Strickland et al, further work needs to be done to establish this conclusively. We need to identify these rates for other values of Γ_c and collect multiple experimental runs to ensure the findings. In Figure 6.11a we see the height of the distension against time for different values of Γ_0 and in Figure 6.11b we see the calculation of the rate of decay.

6.1.5 Outward Spreading Simulations

In addition our exploration of inward spreading simulations, we also studied the outward spreading case, albeit in not as much depth as inward spreading. The surfactant and height profiles of the multilayer equation of state and the empirical equation of state are presented in Figures 6.12a and 6.12b and Figures 6.13a and 6.13b respectively. As before, we begin with some observations about the qualitative differences between the profiles produced by the two EoS.

Surfactant Profiles

Like in the case of the inward spreading of surfactant, there are important qualitative differences between the profiles obtained from the empirical and multilayer EoS. These are discussed below.

First, we see that the amount of surfactant in the center drops considerably faster in the case of the empirical equation of state as opposed to the multilayer equation of state. However, the leading edge of the surfactant moves outward faster in the case of the multilayer EoS. It is important to note that the total surfactant present is approximately the same over all time for both runs, though it might appear so. We reconcile these two seemingly conflicting observations by noticing that, as with the inward spreading surfactant profiles, the two EoS interact differently with the steep gradient in initial surfactant concentration. The empirical EoS maintains the sharp gradient as it spreads outward, while the gradient gets smoothened in the case of the multilayer EoS. This behavior is consistent with what we

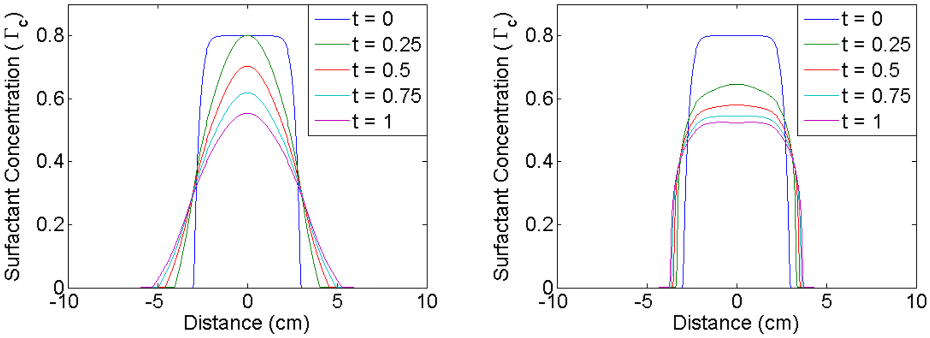

a. The surfactant profiles of an outward spreading run starting with $\Gamma_0 = 0.8\Gamma_c$ at times t = 0, 0.25, 0.5, 0.75 and 1 second using the multilayer EoS. Notice the box-like shape of the profiles, and the rate at which the peak surfactant concentration drops.

b. The surfactant profiles of an outward spreading run starting with $\Gamma_0 = 0.8\Gamma_c$ at times t = 0, 0.25, 0.5, 0.75 and 1 second using the empirical EoS. Notice the profiles are now more diffuse, the peak position drops relatively slowly and the surfactant spreads outward faster.

Figure 6.12 Surfactant profiles for the multilayer and empirical EoS.

noticed in the inward spreading simulations.

It is interesting to note that the initial dynamics for the empirical simulation is very fast—the central surfactant concentration drops to about $0.6\Gamma_c$ in 0.25 seconds, while after that it slows down considerably. This is another instance of the system beginning in region B of the EoS and then moving to region A. Furthermore, it appears that in the long term, whatever surfactant concentration we begin with, (since we are spreading outward with a relatively small total amount of surfactant in relation to the size of the domain), the system would make the transition from region B to region A. This would not happen in the case of the multilayer EoS, and so at long times, we expect the profiles simulated using the multilayer EoS to display faster dynamics than those seen in profiles generated using the empirical EoS.

Height Profiles

Much like with the surfactant profiles, we see some important qualitative differences between the height profiles produced by the two EoS.

The first major difference one notices is that the behavior at the center is widely different. The height at the center drops considerably faster in

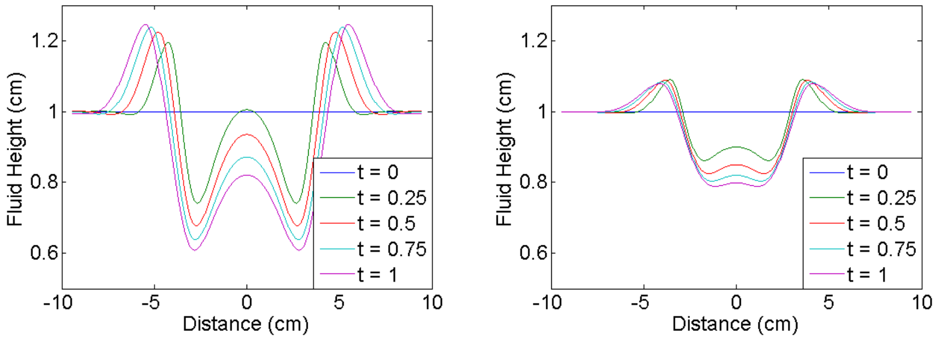

a. The height profiles of an outward spreading run starting with $\Gamma_0 = 0.8\Gamma_c$ at times t = 0, 0.25, 0.5, 0.75 and 1 second using the multilayer EoS. We see an anular Marangoni ridge spreading outward while the height at the center decreases rather quickly. The height of the ridge is also considerably less than in the multilayer case.

b. Theheight profiles of an outward spreading run starting with $\Gamma_0 = 0.8\Gamma_c$ at times t = 0, 0.25, 0.5, 0.75 and 1 second using the empirical EoS. The anular Marangoni ridge is very similar to that of the simulations using the empirical EoS. The behavior at the center is however markedly different.

Figure 6.13 Height profiles for the multilayer and empirical EoS.

the case of the empirical EoS as opposed to the multilayer EoS. Second, the height of the Marangoni ridge is also considerably higher in the case of the multilayer EoS. This is possibly because the simulations that use the empirical EoS spend very little time in region B. Hence the $\nabla\sigma(\Gamma)$ term is non zero for a very short period of time, unlike with the multilayer EoS. We notice a similar transition from region B to region A here as well—the first quarter second has quick dynamics, followed by very slow dynamics.

Leading Edge of the Surfactant

The visual comparisons between the two EoSs suggested that the leading edge of the surfactant is one property which considerably differs between the two EoS. We want to compare our results against those of Swanson et al.; hence we use the same initial surfactant concentrations of $0.13, 0.21, 0.26$ and $0.30\Gamma_c$ even though they are all in region A Swanson et al. (2013). The position of the leading edge of the surfactant under the empirical EoS, plotted against time is presented in Figure 6.14a. The fact that the leading edge appears to be stationary for a certain amount of time following which it makes a discontinuous jump to the next position is an artifact of the spatial

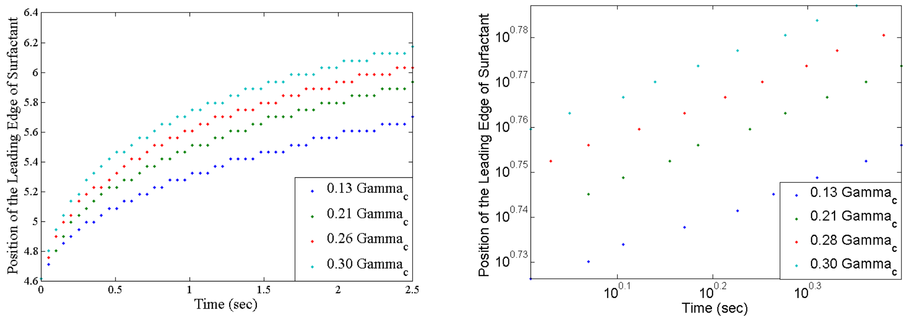

a. The position of the leading edge against time for for Γ_0 = 0.13, 0.21, 0.26 and $0.30\Gamma_c$. The discontinuities are an artifact of the spatial discretization.

b. Log log plot of the leading edge of the surfactant against time for Γ_0 = 0.13, 0.21, 0.26 and $0.30\Gamma_c$. The slopes are all between 0.25 and 0.28.

Figure 6.14 Analyzing the leading edge of surfactant for the empirical EoS in outward spreading runs.

discretization. A finer grid should get rid of this issue. In addition to the position of the leading edge, we also identify the spreading rate defined to be α such that $r_s \propto t^{\alpha}$ where r_s is the position of the leading edge. We do this by calculating the slope of the linear relation we would see on a log-log plot of the leading edge of the surfactant against time. As a result of the discontinuous progression of the leading edge, we cannot directly fit a linear relation to the log-log data. To identify the slope, we take only the first instance of the leading edge at a particular distance. Since the repeats at later times are due to lack of spatial resolution, it is clear that those positions are not accurate. Furthermore, we also throw out data for $t < 1$ second to avoid an initial transient regime that is affected by the specifics of the initial condition. The slopes we extract for all 4 initial surfactant concentrations (betwen 0.13 and $0.4\Gamma_c$) are around 0.27. This agrees with the theoretical estimate of 0.25 and the experimental results presented by Swanson et al Swanson et al. (2013).

6.1.6 Investigating the Behavior of the Model with Large Γ_0

In addition to exploring the difference between the profiles generated by the two equations of state, we also notice different behavior at $\Gamma_0 < \Gamma_c$ and $\Gamma_0 > \Gamma_c$. We need to keep in mind that our model was derived assuming a monolayer, so we do not know how applicable the model's predictions are.

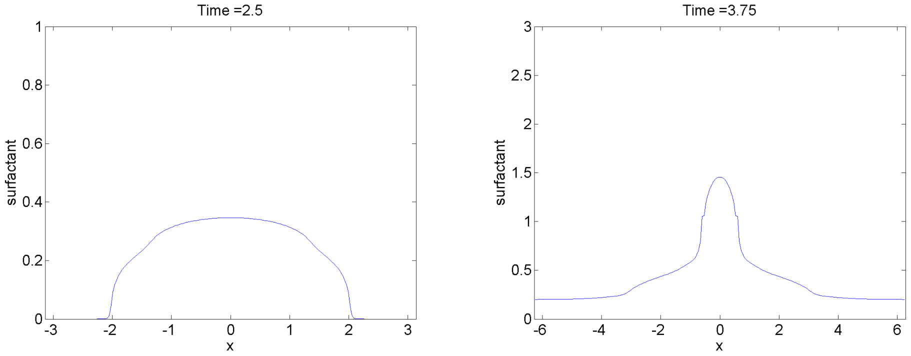

a. The surfactant profile of an outward spreading run with an initial surfactant concentration of Γ_c. We note that the profile is not qualitatively different from profiles below Γ_c.

b. The surfactant profile of an outward spreading run with an initial surfactant concentration of 3 Γ_c. We note that the profile is qualitatively different from profiles below Γ_c - we see a central reservoir of surfactant.

Figure 6.15 Outward spreading runs for $\Gamma_0 = \Gamma_c$ and $\Gamma_0 = 3\Gamma_c$

Nonetheless, the presence of qualitatively different behaviors in the two regimes is interesting in and of itself, since this qualitative difference is only present with the empirical EoS, and not with the multilayer EoS. In Figure 6.15a and Figure 6.15b we have two examples of the the near-time behavior of the surfactant concentration profiles with a empirical EoS in an outward spreading run. The first figure presents the results with $\Gamma_0 = 1\Gamma_c$ while in the second case $\Gamma_0 = 3\Gamma_c$. In Figure 6.15a, the surfactant just dissipates in a rather uniform manner, much like when $\Gamma_0 < \Gamma_c$. In Figure 6.15b, we see the second case where $\Gamma_0 = 3\Gamma_c$. A leading edge of surfactant emerges and the central region becomes a reservoir, with the entire profile assuming a 'sombrero-like' shape before ultimately dissipating in the same way as in the first case. The presence of this leading leg for such large values of Γ_0 is interesting since a similar phenomenon is observed in the experiments, although the experiments have a leading leg for $\Gamma_0 < \Gamma_c$ [2]. The lack of the leading edge seen in experimental outward spreading runs for $\Gamma_0 < \Gamma_c$ is an important drawback of our model [3]. It is not entirely clear why this leading edge is produced though it is probably because the regime transition from region B to region C at Γ_c. Further study of this phenomenon is necessary to completely understand the behavior of the empirical EoS, and could inform our efforts to reproduce the leading leg of surfactant (in the model) for smaller values of Γ_0 as well.

---

[2] Note that these simulations have been done on a square grid of size 4π to avoid the Marangoni ridge running into the boundary

[3] These simulations were run with a tanh-shaped EoS, though not with the exact parameters of the fitted empirical EoS.

Chapter 7

Conclusion

7.1 Summary of Results

In this thesis we considered the effect of an empirical equation of state in the hope that there would be greater agreement between the predictions of the thin-film surfactant model and experimental observations. Specifically, we compared the results produced by the empirical EoS with those of the multilayer EoS. We noticed two important differences between the two EoSs.

First, the empirical EoS preserves steep surfactant gradients while the multilayer EoS smoothens out such gradients relatively quickly. This is an improvement on the model since experimental observations show that steep surfactant concentration gradients are preserved. Second we see that dynamics caused by the empirical EoS can fall in different regimes depending on the surfactant concentration. This is another feature that is not present in the simulations generated using the multilayer EoS. However Strickland et al's data is suggestive of the regime shift in experimental observations as well (Strickland et al., 2014). This however is far from conclusive and needs to be studied in much greater detail. The empirical EoS retains good predictions on the surfactant spreading rates, which the multilayer EoS had as well. However, the rate of decay of the central distension in inward spreading runs appears to be far slower in the case of the empirical EoS. This is another avenue of further exploration. In addition, we have studied region A and region B of the empirical EoS but have only considered region C in passing. In order to fully understand the impact of the empirical EoS, this is another avenue that needs to be explored.

7.2 Future Work

While the empirical EoS improves the model's agreement with experiment, important discrepancies remain. In this section, we look at two avenues of future work—simulations that could help improve our understanding and further experimentation that could help fully determine the effectiveness of the empirical EoS in modeling the system.

7.2.1 Simulations

There are four avenues for further research that can be aided by new simulations.

Region C of the Empirical EoS

First, we have not really explored region C of the empirical EoS. Preliminary results suggested that there might be significantly different behavior in region C, but we need to run simulations for a varied set of surfactant concentrations (I would recommend 1.2, 5 and 10 Γ_c). We saw how this region of the EoS might affect outward spreading runs but have not yet considered the inward spreading case.

Timescale Issues

Strickland et al identified time scale issues to be a predominant concern with the profiles produced by the multilayer EoS (Strickland et al., 2014). The empirical EoS does not affect the time scale in a simple manner—the precise impact seems to depend on the regime the dynamics are in; the fact the dynamics can transition from one regime to another in a single run further complicates this issue. Filling out the simulations for many different values of Γ_0 (less than Γ_c) would us understand this issue better.

Meniscus Effects

Although the empirical EoS improves the agreement with experiment of the surfactant profiles, there is still one major discrepancy between the simulated and experimentally observed surfactant profiles—there is an surfactant ridge in experimental inward spreading runs which we do not see in the simulations. The present hypothesis is that this caused due to a meniscus forming in the experiments. Running simulations with a meniscus in the initial condition might help clarify this issue.

Different Functional Forms for the EoS

An important approximation we made in the modeling process was to fit a tanh to experimental data of the EoS. The exact choice of the fitting function is important since functions with similar shapes could have vastly different derivatives. For example, it would be interesting to see how the results change with a piecewise linear approximation instead of a tanh fit.

7.2.2 Experimental Runs

In addition to more simulations, experimental verification of the validity of the empirical EoS is important. There are four categories of experimental runs that would help gauge the effectiveness of the empirical EoS.

Regime Changes

An important prediction of the empirical EoS is that there are distinct regimes with different dynamics. One way to verify this would be to conduct experiments that test the behavior peculiar to these regimes. For example, an experiment where the inside and the outside of the ring have surfactant concentrations that are different but in region A would be useful. The empirical EoS would predict that diffusion would be the primary method of motion for the surfactant, so the time scale would be much slower than if one of the regions (or both regions) had surfactant concentrations in region B.

EoS Data

The EoS data was collected by Strickland on a Langmuir trough which is a thick film. It is unclear if the thickness of the film affects this relation, so verifying the data on a thin film would be very helpful.

Experiments at Large Γ_0

We also want to test the validity of the model for $\Gamma_0 > \Gamma_c$. While we do not expect the model to be accurate in this region, it would be interesting to see how the experiments compare to the simulations for such high surfactant concentrations.

Filling out the Parameter Space

Like with the simulations, we have experimental data for a limited number of initial surfactant concentrations. More data will allow us to make better comparisons, especially with characteristics like the spreading and decay rates. Furthermore, we also need repetitions at each value of Γ_0 so we obtain error ranges on the experimental data.

Appendix A

Defining the Problem for the Implicit Solver

This description will be focused on the Surfactant equations (and not any fourth order system in general). There are six key components to the defining the surfactant-thin film system.

- Defining system parameters—This is handled in *setrun.py*, a python wrapper function. All system parameters such as β, δ and κ are set here. Apart from this, the grid size, time step, end time, mesh size, grid location and other run parameters are also defined. Importantly, the type of boundary condition is also specified in this wrapper function. For our runs so far we use the following values for β, δ and κ:
$$\beta \approx 1 \qquad \delta \approx 10^{-4} \qquad \kappa \approx 10^{-2}$$

- Implementing the boundary conditions—This is handled in the file *setimplicitboundarydata.f90*. This file specifies the boundary conditions in the format described in *setrun.py*. If the boundary conditions are set to be periodic or there are no boundary conditions (out flow condition), then nothing needs to be specified. Else, the boundary condition can involve any combination of the height or its three derivatives, and the surfactant concentration or its derivative. Note that two conditions need to be specified for the height while one needs to be specified for the surfactant concentration.

- Implementing the intial conditions—This is handled in the file *qinit.f90*. The default initial condition is to have a planar region of liquid with surfactant on it and an adjacent region with no liquid or surfactant on it. Changing this initial condition to a radial initial condition has proven difficult. Simple changes to the initial conditions, such as making the height profile uniform, are causing Newton's method to not converge. So far we have got only two sets of initial conditions to work—the default where a half plane of fluid spreads and second where both the height and the surfactant concentration are constant. The fact that we are having so much difficulty changing the initial conditions suggests that either we are implementing the boundary conditions incorrectly, or there are some deeper problems within the code.

- Calculating the fluxes—This is the part of the program where the governing equations get encoded; this is done in *applypdeoperator*. The fluxes are calculated at the center of each grid cell by calculating h_t and Γ_t to the left and right. These are then subtracted to obtain the flux. We notice that the β term is missing in the calculation of the surfactant flux. We believe this to be an error, though it does not explain the convergence issues.

- Incorporating the equation of state: This is handled in *surfacetensionutils.f90*. This is a simple file where the user inputs the required equation of state and its derivative. The defaults are a linear and inverse cubic EOS. I have added in a tanh EOS as well.

- Plotting and setting run paramters: There are no built in plotting methods. I used plotting tools developed by Eric Autry in Matlab Autry et al. (2011). I believe that the Clawpack plotting libraries such as plotclaw2 can be used as well though this requires an auxiliary file *setplots.py* which is not provided.

Bibliography

Autry, Eric, Cameron Conti, and Greg Kronmiller. 2011. Numerical simulations of surfactant spreading on a thin liquid film.

Claridge, Jonathan, Rachel Levy, and Jeffrey Wong. 1990. Implementation of non-linear implicit pde solvers: Techniques and a clawpack library. *J Fluid Mech* 213(1):127–148.

Craster, RV, and OK Matar. 2006. Numerical simulations of fingering instabilities in surfactant-driven thin films. *Physics of Fluids* 18:032,103.

Gaver, Donald P, and James B Grotberg. 1990. The dynamics of a localized surfactant on a thin film. *J Fluid Mech* 213(1):127–148.

Jensen, Olivier. 1994. Self-similar, surfactant-driven flows. *Physics of Fluids* 6:1084.

Lyzenga, Gregory, and Andrew Bernoff. 2013. *Fields and Waves*. Harvey Mudd College.

Megson, Peter. 2014. Experiments on surfactant on thin fluid films. Harvey Mudd College Senior Thesis.

Strickland, Stephen, Matthew Hinn, Richard Sayanagi, Cameron , Gaebler, Karen Daniels, and Rachel Levy. 2014. Self-healing dynamics of surfactant coatings on thin viscous films. *Physics of Fluids* .

Swanson, Ellen. 2010. Flow of thin liquid films with surfactant: Analysis, numerics, and experiment. *PhD Thesis* .

Swanson, Ellen, Stephen Strickland, Michael Shearer, and Karen Daniels. 2013. Surfactant spreading on a thin liquid film: Reconciling models and experiments. URL http://arxiv.org/abs/1306.4881.

Tsukanova, Valeria, David Grainger, and Christian Salesse. 2002. Monolayer behavior of nbd-labeled phospholipids at the air/water interface. *Langmuir* .